

Review article

Time-dependent cracking and brittle creep in crustal rocks: A review

N. Brantut^{a,*}, M.J. Heap^b, P.G. Meredith^a, P. Baud^b^a Rock and Ice Physics Laboratory (RIPL), Department of Earth Sciences, University College London, Gower Street, London WC1E 6BT, UK^b Laboratoire de Déformation des Roches, Géophysique Expérimentale, Institut de Physique de Globe de Strasbourg (UMR 7516 CNRS, Université de Strasbourg/EOST), 5 rue René Descartes, 67084 Strasbourg cedex, France

ARTICLE INFO

Article history:

Received 17 September 2012

Received in revised form

6 February 2013

Accepted 18 March 2013

Available online 11 April 2013

Keywords:

Brittle creep

Stress corrosion

Rock deformation

Experimental

Long-term strength

Static fatigue

ABSTRACT

Rock fracture under upper crustal conditions is driven not only by applied stresses, but also by time-dependent, chemically activated subcritical cracking processes. These subcritical processes are of great importance for the understanding of the mechanical behaviour of rocks over geological timescales. A macroscopic manifestation of time-dependency in the brittle field is the observation that rocks can deform and fail at constant applied stresses, a phenomenon known as brittle creep. Here, we review the available experimental evidence for brittle creep in crustal rocks, and the various models developed to explain the observations. Laboratory experiments have shown that brittle creep occurs in all major rock types, and that creep strain rates are extremely sensitive to the environmental conditions: differential stress, confining pressure, temperature and pore fluid composition. Even small changes in any of these parameters produce order of magnitude changes in creep strain rates (and times-to-failure). Three main classes of brittle creep model have been proposed to explain these observations: phenomenological, statistical, and micromechanical. Statistical and micromechanical models explain qualitatively how the increasing influence of microcrack interactions and/or the increasing accumulated damage produces the observed evolution of macroscopic deformation during brittle creep. However, no current model can predict quantitatively all of the observed features of brittle creep. Experimental data are limited by the timescale over which experiments are realistically feasible. Clearly, an extension of the range of available laboratory data to lower strain rates, and the development of new modelling approaches are needed to further improve our current understanding of time-dependent brittle deformation in rocks.

Crown Copyright © 2013 Published by Elsevier Ltd. All rights reserved.

1. Introduction and theoretical background

Under upper crustal conditions most rocks accommodate deformation in a brittle manner through fracturing and faulting. The general view is that brittle failure is achieved once some critical stress is reached; either the stress needed to generate a new fracture in intact rock, or that required to slide along a pre-existing interface or shear fault (e.g., Paterson and Wong, 2005; Scholz, 2002). Even such frictional sliding along pre-existing faults requires the breakage of asperities at various scales (from the grain-size to crustal-scale fault jogs), and the fracturing of previously-healed fault segments (e.g., Sibson, 1986). The fracture stress of rocks is hence a key parameter controlling the dynamics of the brittle upper crust. Among the many factors affecting the brittle strength of rocks, time (or, equivalently, strain rate) is the least well understood. However, quantifying time-dependent rock

deformation is crucial to unravelling the complexities of the evolution and dynamics of the brittle crust. For instance, the presence of cracks allows crustal rocks to store and transport fluids, and even modest changes in crack size, density, or linkage can produce major changes in fluid transport properties. Time-dependent rock deformation therefore has both a scientific and a socio-economic impact since it controls the precursory phase of important geohazards such as earthquake rupture (Main and Meredith, 1991) and volcanic eruptions (Main, 1999; Heap et al., 2011), and also influences effective recovery of hydrocarbon and geothermal energy resources (Cornet et al., 2007), the integrity of underground mines and excavations (Diederichs and Kaiser, 1999) and the long-term storage of hazardous waste (Nara et al., 2010) and CO₂ (Trippetta et al., 2013). Our current lack of understanding in this area has recently been highlighted by UNESCO, and “Understanding Slow Deformation before Dynamic Failure” was one of the two priority areas for study within the Natural Hazards theme of its International Year of Planet Earth (Ventura et al., 2010).

The goal of this review is to summarize our current knowledge of time-dependent fracturing and brittle creep of rocks. A major

* Corresponding author.

E-mail address: nicolas.brantut@normalesup.org (N. Brantut).

challenge in this field is to understand how, and to what extent, microscopic (grain scale) time-dependent crack growth processes are linked to the observed macroscopic mechanical behaviour of rocks. In order to discuss these issues, in the remainder of the introduction we will recall the key concepts underlying our understanding of brittle fracture, and then introduce the physico-chemical mechanisms responsible for time-dependent crack growth.

1.1. Propagation of single cracks in rocks

Crustal rocks generally contain finite porosity comprising some combination of open pores between grains, triple-junction voids between crystalline phases, grain boundary voids and open microcracks, even at considerable depth (see review by Kranz, 1983). These defects act as stress concentration points from which cracks can nucleate and propagate. Above some threshold density, such cracks will interact and coalesce until eventually macroscopic failure ensues, commonly via the generation of a shear fault. Therefore, in order to understand the micromechanics of brittle failure controlled by crack growth, it is useful to replace the concept of a critical stress controlling brittle strength with the concept of a critical stress concentration controlling crack propagation.

Following the pioneering work of Griffith (1921), Irwin (1958) showed that by measuring the force required to cause unstable propagation of a crack of known length and geometry it was possible to determine the fracture resistance of any material. Lawn (1993) gives a complete analysis of the manner in which the presence of cracks modifies the local stress and displacement fields in a stressed elastic solid, and provides a general expression for the near-field stress distribution of the form:

$$\sigma_{ij} = K \cdot r^{-0.5} \cdot f_{ij}(\theta) \quad (1)$$

where, σ_{ij} is the stress tensor, and r and θ are the radial distance from the crack tip and the angle measured from the crack plane, respectively. The coefficient K is known as the *stress intensity factor*; and describes the magnitude or intensity of the local driving stress close to the crack tip. In laboratory configurations for the experimental determination of fracture parameters, it is usual to simplify the analysis by arranging for uniform loading of a two-dimensional tensile (mode I; Lawn, 1993) crack. Under these conditions, the tensile stress intensity factor K_I is given by:

$$K_I = B\sigma_r\sqrt{\pi l}, \quad (2)$$

where, σ_r is the remotely applied tensile stress and l is the crack half-length. B is a dimensionless parameter that describes the crack and loading geometry, and has been tabulated for a wide range of crack configurations (e.g., Sih, 1973; Tada et al., 1973). Classical linear elastic fracture mechanics predicts that a crack will propagate dynamically at some terminal velocity close to the Rayleigh wave speed once some critical value of K_I , known as the *fracture toughness* (K_{IC}) is exceeded. K_{IC} therefore describes the resistance of the rock to dynamic fracture propagation. At values below the critical value, pre-existing cracks should remain stable and stationary.

This simple, dynamic fracture criterion is, however, generally found to be inadequate to describe fully crack growth in most rocks. A commonly observed characteristic of crustal rocks is that their fracture resistance depends strongly on the environmental conditions under which the deformation takes place, and also upon the rate of deformation. This is especially true at elevated temperature and in the presence of chemically reactive pore fluids. A

considerable body of experimental evidence supports the idea that cracks can propagate in a stable, quasi-static manner at values of K_I well below the critical value, K_{IC} , albeit at velocities that are orders of magnitude lower than the terminal velocity associated with catastrophic, dynamic rupture. This phenomenon is known as *subcritical crack growth* and has been reported for a wide range of rock types including sandstones, limestones, granites and basalts amongst others (e.g., see the data compilation of Atkinson and Meredith, 1987a), as well as engineering materials such as glass and ceramics (e.g., Lawn, 1993, Chapter 5). There exists a whole range of micro-mechanisms that could be responsible for subcritical crack growth (reviewed in Atkinson and Meredith, 1987b), including atomic diffusion, dissolution, ion exchange, micro-plasticity and stress corrosion. Nevertheless, the overwhelming body of experimental and observational evidence suggests that growth of pre-existing cracks and flaws by the mechanism of stress corrosion is the dominant mechanism of subcritical crack growth in rocks under conditions prevailing in the upper crust (Anderson and Grew, 1977; Atkinson, 1982, 1984; Atkinson and Meredith, 1987b; Costin, 1987).

Stress corrosion describes the fluid–rock reactions that occur preferentially between a chemically active pore fluid and the strained atomic bonds close to crack tips. For example, in the silica–water system, bridging bonds close to crack tips, that are the main stress-supporting components, are replaced by weaker hydrogen bonds, thus facilitating crack growth at lower levels of stress than would otherwise be the case (Michalske and Freiman, 1982, 1983; Freiman, 1984; Hadizadeh and Law, 1991). To date, the vast majority of experimental data on stress corrosion cracking in rocks has been derived from experiments on single, tensile macro-cracks conducted at ambient pressure. Fig. 1 shows log–log plots of the relationship between crack velocity and the tensile stress intensity factor, K_I , from such experiments conducted on samples of Crab Orchard sandstone (from Atkinson, 1980) and Whin Sill dolerite (from Meredith and Atkinson, 1983) at ambient pressure. Clearly, the level of applied K_I exerts a dramatic influence on the measured crack velocity. A number of theoretical formulations have been proposed to describe this relationship (reviewed in Atkinson and Meredith, 1987b; Costin, 1987), which are of the general form

$$v = v_0 \exp\left(\frac{-H}{RT}\right) f(K_I), \quad (3)$$

where, v_0 is the limiting lower velocity for stress corrosion crack growth, H is the activation enthalpy of the process, R is the universal gas constant and T is the absolute temperature. The function $f(K_I)$ describes the influence of the stress intensity factor on the crack growth rate. Three formulations are commonly used:

$$f(K_I) = \begin{cases} K_I^n, & (4a) \\ \exp(bK_I/RT), & (4b) \\ \exp(bK_I^2/RT). & (4c) \end{cases} \quad (4)$$

Expression (4a) corresponds to Charles' law (Charles, 1958), in which n is known as the *stress corrosion index* and is a measure of the susceptibility of the rock to subcritical crack growth in the particular environment of the measurement. Although purely empirical, this formulation has been widely used to describe subcritical crack growth in rocks (Atkinson, 1984). Expressions (4b) and (4c) are exponential forms parameterised by a factor b , and have been derived from reaction rate theory (see for instance Freiman, 1984; Darot and Guéguen, 1986; Wan et al., 1990). In the formulation (4b) (e.g., Freiman, 1984), b is proportional to the crack tip curvature and to the activation volume of the stress corrosion reaction. In the formulation (4c) (e.g., Darot and Guéguen, 1986), b

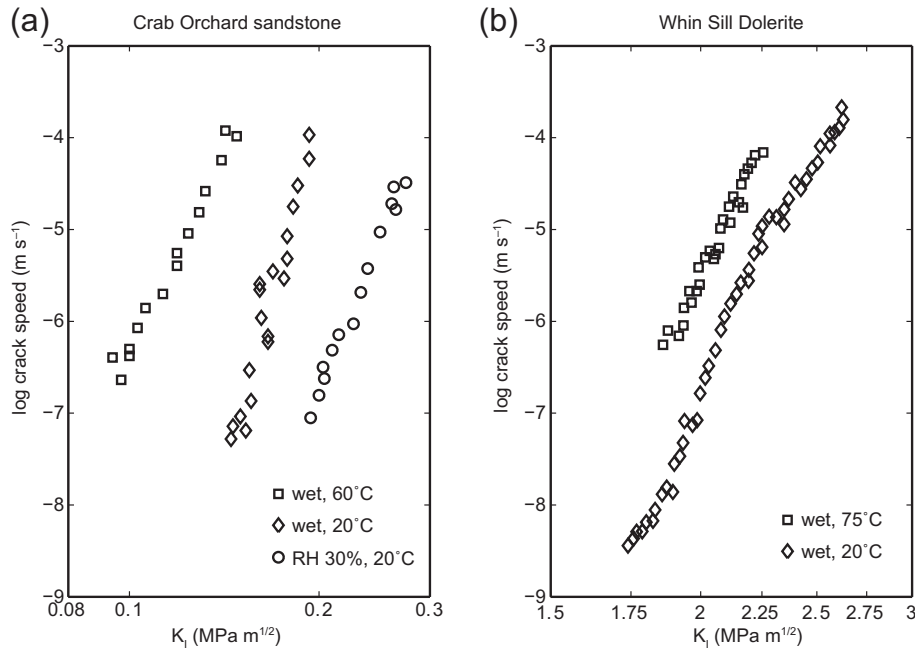


Fig. 1. (a) Plots of crack velocity against stress intensity factor for Crab Orchard sandstone under different conditions (data from Atkinson, 1980). (b) Plots of crack velocity against stress intensity factor for Whin Sill dolerite at 20 (diamonds) and 75 °C (squares) (data from Meredith and Atkinson, 1983).

is proportional to the activation area of the stress corrosion reaction. Despite their differences, the three formulations are essentially indistinguishable when used to describe typical experimental data. Most data on rocks report only the empirical stress corrosion index, which generally lies in the range 10–50 (see data compilation in Atkinson and Meredith, 1987a). This relationship is illustrated in Fig. 1, where the stress corrosion index for Whin Sill dolerite is 29 and for Crab Orchard sandstone ranges between 14 and 26.

Fig. 1a shows the strong dependence of crack velocity on the amount of water available. The velocity increases by 2–3 orders of magnitude for the same value of K_I as the environment is changed from air with 30% relative humidity to liquid water. Both parts of Fig. 1 also show the effect of increasing temperature and the concomitant increase in chemical activity of liquid water. Increases of 40 °C and 55 °C lead to increases in crack velocity in Crab Orchard sandstone and Whin Sill dolerite of three orders and one order of magnitude, respectively.

Inspection of Eqs. (2) and (3) shows that, once nucleated, tensile microcracks can propagate at constant applied stress and accelerate as their lengths increase. Macroscopically, this results in delayed tensile failure under constant applied stress, a phenomenon known as *static fatigue*. This link between stress corrosion of microcracks and macroscopic static fatigue was first reported for failure of silica glass by Wiederhorn and Boltz (1970).

1.2. Time-dependent rock failure in compression

Fracture and failure of rocks subjected to all-round compression, as is the case at depth in the crust, are generally much more complex than the propagation of single tensile cracks, because compressive failure involves successively the nucleation, propagation, interaction and coalescence of large numbers of microcracks. Direct observation of such microcracks (e.g., Tapponnier and Brace, 1976; Kranz, 1980; Wong and Biegel, 1985) suggests strongly that they nucleate from pre-existing flaws (pores, microcracks, inclusions, etc.) and propagate primarily as tensile cracks in a

direction parallel to the maximum principal stress. Furthermore, water and aqueous solutions are ubiquitous in the upper crust and, below a few hundred metres, void spaces in most rocks are saturated. It would therefore be surprising if stress corrosion reactions were not also important in compressive failure of rock under upper crustal conditions. It has long been recognized that the compressive strength of rocks is dependent on both environment and strain rate (e.g., Paterson and Wong, 2005). Complementary to the observations of Wiederhorn and Boltz (1970) in glass, Scholz (1968b, 1972) suggested that the mechanism that allowed static fatigue of quartz in compression was stress corrosion. Further evidence was provided by Lankford (1981), who showed that the dependence of the uniaxial compressive strength, σ_{UCS} , of limestone on strain rate, $\dot{\epsilon}$, followed a relationship of the form:

$$\sigma_{UCS} \propto \dot{\epsilon}^{\frac{1}{n^*+1}} \tag{5}$$

where n^* is an environment and material dependent constant for strain rates below about 10^{-2} s^{-1} . Lankford noted that his value of n^* was identical, within experimental accuracy, to the stress corrosion index, n , for the same rock under the same environmental conditions, and argued that, by analogy, compressive failure was controlled by subcritical growth of tensile microcracks. Sano et al. (1981) developed an identical relationship to Eq. (5) for strain rates below 10^{-3} s^{-1} , and reported values of 32 ± 2 and 30 ± 5 for n^* and n , respectively, for Oshima granite.

By far the most common laboratory method for measuring the deformational properties and strength of rocks under conditions relevant to the shallow crust is the *conventional triaxial experiment* conducted under a *constant applied strain rate*. An example of an axial and volumetric stress–strain curve from such an experiment is illustrated in Fig. 2, where, by convention, we denote compressive stresses and strains as positive. Here, a laboratory sample of Darley Dale sandstone (a right cylinder with a length-to-diameter ratio of 2.5:1) has been deformed at a constant rate of 10^{-5} s^{-1} under an effective pressure, P_{eff} , of 30 MPa (resulting from an applied confining pressure of 50 MPa and a pore fluid pressure of

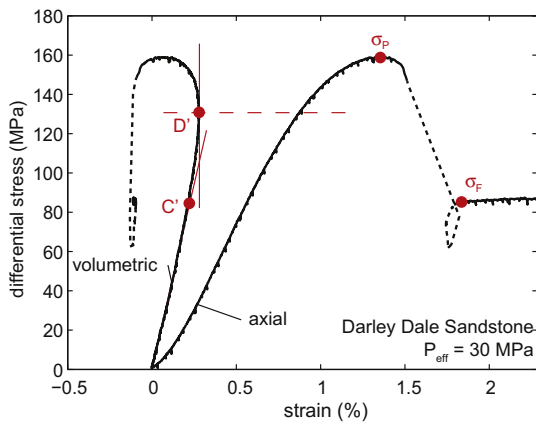


Fig. 2. Stress–strain curve for a sample of Darley Dale sandstone deformed at a constant strain rate of 10^{-5} s^{-1} until failure. The sample was deformed under the conditions of a 50 MPa confining pressure and a 20 MPa pore fluid pressure (yielding an effective pressure of 30 MPa). The positions of C' , D' , σ_p and σ_F are labelled on the curves and are discussed in the text (redrawn after Heap et al., 2009a). Axial strain was measured using a Linear Variable Differential Transformer and volumetric strain was calculated from the sample volume change during deformation.

20 MPa). We observe that the brittle failure process in rock in compression can be broken down into a number of distinct stages (see also Brace et al., 1966; Hoek and Bieniawski, 1965; Scholz, 1968a), characterised by changes in the stress–strain relationship. First, during the initial stage of loading, the axial stress–strain curve exhibits an increasing slope and the volumetric strain is positive. This behaviour can be attributed to axial stiffening of the sample due to the closure of microcracks preferentially aligned normal or sub-normal to the direction of loading, and volume compaction, respectively. Second, the stress–strain behaviour becomes close to linear as the rock deforms quasi-elastically. In the third stage, the slope of the axial stress–strain curve starts to decrease, corresponding to a reduction in stiffness. Simultaneously, this is seen as a deviation from linearity in the volumetric strain, and marks the onset of dilatancy (denoted as C' , as first noted by Brace et al., 1966), as the differential stress becomes high enough to initiate the growth of primarily axial, microcracks. Beyond this point, the volumetric strain eventually reaches a maximum (denoted D'), which marks the transition from compaction-dominated to dilatancy-dominated deformation (see Heap et al., 2009a). This stage continues up to the peak stress (denoted σ_p) with increasing levels of dilatant cracking and volumetric strain. Following the peak stress, in the fourth stage, we observe strain softening that is associated with the coalescence of dilatant microcracks to form a through going shear fault (Lockner et al., 1992; Wu et al., 2000). This is followed by dynamic failure on the fault, but this is commonly very difficult to capture if the testing machine is more compliant than the rock sample (see the dashed lines in Fig. 2 and Cook, 1981). Finally, in a fifth stage, the two parts of the failed sample slide on the shear fault, controlled by the residual frictional stress (denoted σ_F). As noted above, during constant strain rate experiments, samples are brought to failure over short durations at strain rates of around 10^{-5} s^{-1} , much faster than tectonic strain rates that are typically of the order of 10^{-14} – 10^{-15} s^{-1} .

Fast, dynamic deformation in the form of earthquake ruptures and volcanic eruptions do occur in the crust, and rapid deformation experiments (i.e., at a strain rate of 10^{-5} s^{-1}) may be appropriate for studying these critical phenomena. However, earthquake ruptures and volcanic eruptions are actually rare occurrences in both space and time, and most of the crust spends most of its time deforming relatively slowly in a subcritically stressed state. Fast, constant

strain rate experiments are therefore not necessarily the most appropriate means for the study of such time-dependent, subcritical rock deformation over extended durations. An alternative, and more appropriate experimental method is to subject samples to a constant stress that is a high proportion of their short-term strength (peak stress, σ_p , in Fig. 2) and allow them to deform (strain) naturally over time until failure eventually ensues. Such deformation at constant stress is termed *brittle creep*, a process that leads to delayed failure (static fatigue).

In this review, we first describe how time-dependent brittle creep experiments are performed in the laboratory. Then, using a compilation of most of the available published data from triaxial creep experiments on rocks (Tables 1 and 2), we discuss the influence of key parameters on brittle creep: differential stress, effective pressure, temperature, the presence of water, and the rock microstructure. We systematically attempt to establish a link between the observed macroscopic behaviour and the underlying subcritical cracking process. We then present and discuss microstructural observations. The existing theoretical models of brittle creep are then described, and their various strengths and weaknesses discussed. Finally, we present some important implications of time-dependent brittle deformation on the dynamics of faulting and deformation in the Earth's crust.

2. General features of brittle creep and experimental methods

An example of the type of brittle creep experiment introduced above is illustrated in Fig. 3. Here, a sample of Darley Dale sandstone has been loaded at a constant stress rate of 4.5 MPa s^{-1} to a stress of 125 MPa (80% of its short-term strength). The loading was then stopped and the sample allowed to deform under this constant stress (maintained by a servo-control system) until failure occurred after approximately 160 min. This type of creep deformation has commonly been described as exhibiting an apparent trimodal behaviour when creep strain is plotted against time. The three stages of the creep curve are: (1) primary or decelerating creep, (2) secondary or steady-rate creep, and (3) tertiary or accelerating creep (Fig. 3). There is currently some debate as to whether secondary creep exists as a distinct phase or simply as an inflexion between the primary and tertiary phases. This point will be discussed further when we review creep models (Section 5). Secondary creep is defined empirically, and corresponds to the time interval during which the strain rate remains apparently constant; generally known as the *creep strain rate*. Even if secondary creep occurs merely as an inflexion between primary and tertiary creep, the measurement of a brittle creep strain rate is useful because if then defines the *minimum strain rate* achieved during any experiment.

The measurements typically recorded during creep experiments include time, differential stress (although this remains constant), strain (axial, radial, and/or volumetric), porosity change (also a proxy for volumetric strain) and acoustic emission (AE) statistics (number, rate, amplitude, energy, and/or location).

In order to describe fully the brittle creep process it is necessary to perform a suite of creep experiments over a range of imposed creep stresses that are different percentages of the short-term strength (σ_p), yielding a range of different times-to-failure and creep strain rates. In principle, it should be possible to conduct a brittle creep experiment at any stress higher than that required for the onset of dilatant cracking (C' in Fig. 2). However, experiments at stresses close to this lower limit are likely to be extremely slow and therefore impracticable to study over reasonable laboratory time-scales (which have typical durations from a few hours to a maximum of a few weeks). A pragmatic solution to this issue is

Table 1
Summary of brittle creep data for igneous and volcanic rocks under triaxial conditions.

Rock type	Porosity (%)	Differential stress (MPa)	σ_c/σ_p	Effective pressure (MPa)	Pore pressure (MPa)	T (°C)	Creep strain rate (/s)	Time-to-Failure (s)	Reference	Notes and additional information
Barre granite	0.4 ^b	162.0	0.740	0.1	0	RT	—	1,600,000	Kranz (1980)	Axial and radial strains at failure; fracture angle; creep coefficients; crack length analysis
Barre granite	0.4 ^b	173.0	0.790	0.1	0	RT	—	230	Kranz (1980)	
Barre granite	0.4 ^b	177.0	0.800	0.1	0	RT	—	22,900	Kranz (1980)	
Barre granite	0.4 ^b	179.0	0.810	0.1	0	RT	—	1140	Kranz (1980)	
Barre granite	0.4 ^b	185.0	0.840	0.1	0	RT	—	650	Kranz (1980)	
Barre granite	0.4 ^b	188.0	0.850	0.1	0	RT	—	505	Kranz (1980)	
Barre granite	0.4 ^b	196.0	0.890	0.1	0	RT	—	435	Kranz (1980)	
Barre granite	0.4 ^b	199.0	0.900	0.1	0	RT	—	149	Kranz (1980)	
Barre granite	0.4 ^b	203.0	0.920	0.1	0	RT	—	12	Kranz (1980)	
Barre granite	0.4 ^b	252.0	0.870	10	0	RT	—	562	Kranz (1980)	
Barre granite	0.4 ^b	318.0	0.870	25	0	RT	—	10,500	Kranz (1980)	
Barre granite	0.4 ^b	395.0	0.810	53	0	RT	—	355,000	Kranz (1980)	
Barre granite	0.4 ^b	410.0	0.840	53	0	RT	—	159,000	Kranz (1980)	
Barre granite	0.4 ^b	413.0	0.850	53	0	RT	—	122,000	Kranz (1980)	
Barre granite	0.4 ^b	422.0	0.870	55	0	RT	—	12,900	Kranz (1980)	
Barre granite	0.4 ^b	431.0	0.890	55	0	RT	—	29,500	Kranz (1980)	
Barre granite	0.4 ^b	440.0	0.910	53	0	RT	—	3030	Kranz (1980)	
Barre granite	0.4 ^b	450.0	0.930	54	0	RT	—	525	Kranz (1980)	
Barre granite	0.4 ^b	460.0	0.950	53	0	RT	—	252	Kranz (1980)	
Barre granite	0.4 ^b	540.0	0.860	100	0	RT	—	714,000	Kranz (1980)	
Barre granite	0.4 ^b	550.0	0.870	101	0	RT	—	119,000	Kranz (1980)	
Barre granite	0.4 ^b	555.0	0.880	101	0	RT	—	18,400	Kranz (1980)	
Barre granite	0.4 ^b	575.0	0.910	102	0	RT	—	2540	Kranz (1980)	
Barre granite	0.4 ^b	590.0	0.930	100	0	RT	—	1090	Kranz (1980)	
Barre granite	0.4 ^b	760.0	0.870	198	0	RT	—	930,000	Kranz (1980)	
Barre granite	0.4 ^b	775.0	0.890	198	0	RT	—	17,500	Kranz (1980)	
Barre granite	0.4 ^b	790.0	0.910	198	0	RT	—	3650	Kranz (1980)	
Barre granite	0.4 ^b	569.3	—	100	0	200	—	23	Kranz et al. (1982)	
Barre granite	0.4 ^b	561.3	—	100	0	200	—	41	Kranz et al. (1982)	
Barre granite	0.4 ^b	548.6	—	100	0	200	—	475	Kranz et al. (1982)	
Barre granite	0.4 ^b	539.3	—	100	0	200	—	2156	Kranz et al. (1982)	
Barre granite	0.4 ^b	509.1	—	100	0	200	—	12,874	Kranz et al. (1982)	
Barre granite	0.4 ^b	505.6	—	100	0	200	—	27,827	Kranz et al. (1982)	
Barre granite	0.4 ^b	525.0	—	100	0	200	—	29,419	Kranz et al. (1982)	
Barre granite	0.4 ^b	485.3	—	100	0	200	—	860,210	Kranz et al. (1982)	
Inada granite	0.45 ^b	280.0	—	10	0	RT	—	—	Fujii et al. (1999)	
Inada granite	0.45 ^b	289.0	—	10	0	RT	1.54E–09 ^a	140,250 ^a	Fujii et al. (1999)	
Inada granite	0.45 ^b	298.0	—	10	0	RT	2.45E–08 ^a	10,032 ^a	Fujii et al. (1999)	
Inada granite	0.45 ^b	301.0	—	10	0	RT	2.75E–08 ^a	7048 ^a	Fujii et al. (1999)	
Inada granite	0.45 ^b	304.0	—	10	0	RT	1.26E–08 ^a	18,450 ^a	Fujii et al. (1999)	
Inada granite	0.45 ^b	306.0	—	10	0	RT	4.45E–08 ^a	3573 ^a	Fujii et al. (1999)	
Inada granite	0.45 ^b	312.0	—	10	0	RT	1.52E–07 ^a	1100 ^a	Fujii et al. (1999)	
Inada granite	0.45 ^b	315.0	—	10	0	RT	1.54E–07 ^a	1650 ^a	Fujii et al. (1999)	
Inada granite	0.45 ^b	494.0	0.950	40	0	RT	8.73E–08 ^a	—	Maranini and Yamaguchi (2001)	
Inada granite	0.45 ^b	468.0	0.900	40	0	RT	1.78E–09 ^a	—	Maranini and Yamaguchi (2001)	
Inada granite	0.45 ^b	369.0	0.900	20	0	RT	9.00E–10 ^a	—	Maranini and Yamaguchi (2001)	
Inada granite	0.45 ^b	288.0	0.900	10	0	RT	5.10E–10 ^a	—	Maranini and Yamaguchi (2001)	
Inada granite	0.45 ^b	247.0	0.950	5	0	RT	6.32E–09 ^a	—	Maranini and Yamaguchi (2001)	
Inada granite	0.45 ^b	234.0	0.900	5	0	RT	5.85E–10 ^a	—	Maranini and Yamaguchi (2001)	
Westerly granite	0.8 ^b	690.0	—	200	0	410	8.59E–10 ^a	—	Ross et al. (1983)	
Westerly granite	0.8 ^b	690.0	—	200	0	506	1.83E–09 ^a	—	Ross et al. (1983)	
Westerly granite	0.8 ^b	690.0	—	200	0	600	3.28E–09 ^a	—	Ross et al. (1983)	
Westerly granite	0.8 ^b	690.0	—	200	0	627	4.63E–09 ^a	—	Ross et al. (1983)	
Westerly granite	0.8 ^b	690.0	—	200	0	657	6.98E–09 ^a	—	Ross et al. (1983)	
Westerly granite	0.8 ^b	690.0	—	200	0	737	1.40E–08 ^a	—	Ross et al. (1983)	
Westerly granite	0.8 ^b	690.0	—	200	0	769	2.17E–08 ^a	—	Ross et al. (1983)	
Westerly granite	0.8 ^b	170.0	—	10	5 (0.01 M KCl)	28.5	3.03E–09 ^a	—	Lockner and Byerlee (1986)	
Westerly granite	0.8 ^b	747.0	0.983	50	0	RT	—	69	Kurita et al. (1983)	
Westerly granite	0.8 ^b	741.0	0.975	50	0	RT	—	106	Kurita et al. (1983)	
Westerly granite	0.8 ^b	736.0	0.969	50	0	RT	—	1059	Kurita et al. (1983)	
Westerly granite	0.8 ^b	733.0	0.965	50	0	RT	—	10,132	Kurita et al. (1983)	
Westerly granite	0.8 ^b	730.0	0.961	50	0	RT	—	11,442	Kurita et al. (1983)	
Westerly granite	0.8 ^b	725.0	0.955	50	0	RT	—	19,739	Kurita et al. (1983)	
Westerly granite	0.8 ^b	715.0	0.941	50	0	RT	—	151,560	Kurita et al. (1983)	

(continued on next page)

Table 1 (continued)

Rock type	Porosity (%)	Differential stress (MPa)	σ_C/σ_P	Effective pressure (MPa)	Pore pressure (MPa)	T (°C)	Creep strain rate (/s)	Time-to-Failure (s)	Reference	Notes and additional information	
Westerly granite	0.84	392.2	0.736	30	20	RT	5.33E-09	–	Brantut et al. (2012)	Micromechanical model	
Westerly granite	0.84	399.5	0.750	30	20	RT	6.91E-09	–	Brantut et al. (2012)		
Westerly granite	0.84	408.5	0.766	30	20	RT	2.34E-08	–	Brantut et al. (2012)		
Westerly granite	0.84	424.3	0.796	30	20	RT	4.27E-08	–	Brantut et al. (2012)		
Westerly granite	0.84	434.5	0.815	30	20	RT	9.89E-08	–	Brantut et al. (2012)		
Westerly granite	0.84	450.9	0.846	30	20	RT	1.73E-07	–	Brantut et al. (2012)		
Westerly granite	0.84	466.2	0.875	30	20	RT	2.20E-07	–	Brantut et al. (2012)		
Westerly granite	0.84	484.9	0.910	30	20	RT	3.81E-07	–	Brantut et al. (2012)		
Westerly granite	0.84	494.7	0.928	30	20	RT	8.14E-07	–	Brantut et al. (2012)		
Westerly granite	0.8 ^b	751.3	–	100	0	200	–	180	Kranz et al. (1982)		Axial and radial strains at failure; creep coefficients
Westerly granite	0.8 ^b	730.0	–	100	0	200	–	6515	Kranz et al. (1982)		
Westerly granite	0.8 ^b	699.7	–	100	0	200	–	49,310	Kranz et al. (1982)		
Westerly granite	0.8 ^b	679.5	–	100	0	200	–	349,260	Kranz et al. (1982)		
Westerly granite	0.8 ^b	709.7	–	100	0 (wet)	200	–	385	Kranz et al. (1982)		
Westerly granite	0.8 ^b	695.1	–	100	0 (wet)	200	–	461	Kranz et al. (1982)		
Westerly granite	0.8 ^b	664.4	–	100	0 (wet)	200	–	6620	Kranz et al. (1982)		
Westerly granite	0.8 ^b	624.2	–	100	0 (wet)	200	–	165,330	Kranz et al. (1982)		
Ralston intrusive	–	744.0	0.972	50	0	RT	–	64	Kurita et al. (1983)	Surface deformation	
Ralston intrusive	–	729.0	0.953	50	0	RT	–	545	Kurita et al. (1983)		
Ralston intrusive	–	719.0	0.940	50	0	RT	–	2067	Kurita et al. (1983)		
Ralston intrusive	–	704.0	0.920	50	0	RT	–	110,100	Kurita et al. (1983)		
Takidani granite	1.1	373.3	0.760	30	20	RT	2.34E-08	–	This study	–	
Takidani granite	1.1	381.0	0.776	30	20	RT	3.00E-08	–	This study	–	
Takidani granite	1.1	387.7	0.790	30	20	RT	4.27E-08	–	This study	–	
Takidani granite	1.1	397.0	0.809	30	20	RT	9.00E-08	–	This study	–	
Takidani granite	1.1	404.0	0.823	30	20	RT	1.00E-07	–	This study	–	
Takidani granite	1.1	412.0	0.839	30	20	RT	1.73E-07	–	This study	–	
Takidani granite	1.1	418.0	0.851	30	20	RT	1.78E-07	–	This study	–	
Takidani granite	1.1	426.0	0.868	30	20	RT	2.20E-07	–	This study	–	
Takidani granite	1.1	433.0	0.882	30	20	RT	3.00E-07	–	This study	–	
Takidani granite	1.1	443.0	0.902	30	20	RT	3.81E-07	–	This study	–	
Takidani granite	1.1	452.0	0.921	30	20	RT	6.00E-07	–	This study	–	
Fangshan granite	–	820.0	–	200	0	200	2.71E-07 ^a	–	Kie et al. (1989)	Volumetric strain	
Fangshan granite	–	730.0	–	200	0	200	6.81E-08 ^a	–	Kie et al. (1989)		
Champion Reefs amphibolite	–	570.0	0.850	30	0	RT	–	6840 ^a	Satoh et al. (1996)	AE location; radial strain; volumetric strain	
Etna basalt	4.15	304.4	0.787	30	20	RT	2.40E-09	270,000	Heap et al. (2011)	AE; power law model for tertiary creep; application to volcanology; microstructure	
Etna basalt	4.21	329.4	0.851	30	20	RT	4.00E-08	15,000	Heap et al. (2011)		
Etna basalt	4.17	357.3	0.923	30	20	RT	4.10E-07	1500	Heap et al. (2011)		
Etna basalt	4.22	374.7	0.968	30	20	RT	2.70E-06	270	Heap et al. (2011)		
Etna basalt	4.19	340.1	0.879	30	20	RT	7.80E-08	–	Heap et al. (2011)		
Etna basalt	4.19	335.7	0.867	30	20	RT	5.26E-08	–	Heap et al. (2011)		
Etna basalt	4.19	327.2	0.845	30	20	RT	3.00E-08	–	Heap et al. (2011)		
Etna basalt	4.19	320.8	0.829	30	20	RT	1.62E-08	–	Heap et al. (2011)		
Etna basalt	4.19	312.9	0.809	30	20	RT	7.02E-09	–	Heap et al. (2011)		
Etna basalt	4.19	346.8	0.896	30	20	RT	1.60E-07	–	Heap et al. (2011)		
Etna basalt	4.2	243.0	0.835	10	20	RT	4.72E-08	–	Heap et al. (2011)		
Etna basalt	4.2	247.4	0.850	10	20	RT	1.39E-07	–	Heap et al. (2011)		
Etna basalt	4.2	253.2	0.870	10	20	RT	5.89E-07	–	Heap et al. (2011)		
Etna basalt	4.2	262.1	0.901	10	20	RT	5.74E-06	–	Heap et al. (2011)		
Etna basalt	4.2	260.0	0.893	10	20	RT	2.13E-06	–	Heap et al. (2011)		
Etna basalt	4.23	410.1	0.814	50	20	RT	1.29E-08	–	Heap et al. (2011)		
Etna basalt	4.23	418.0	0.829	50	20	RT	1.77E-08	–	Heap et al. (2011)		
Etna basalt	4.23	425.8	0.845	50	20	RT	2.80E-08	–	Heap et al. (2011)		
Etna basalt	4.23	435.0	0.863	50	20	RT	5.06E-08	–	Heap et al. (2011)		
Etna basalt	4.23	442.0	0.877	50	20	RT	7.93E-08	–	Heap et al. (2011)		
Etna basalt	4.23	460.2	0.913	50	20	RT	2.32E-07	–	Heap et al. (2011)		
Etna basalt	4.18	315.0	–	30	20	75	2.00E-08	–	This study	–	
Etna basalt	4.18	324.0	–	30	20	75	4.11E-08	–	This study	–	
Etna basalt	4.18	333.0	–	30	20	75	7.62E-08	–	This study	–	
Etna basalt	4.18	345.2	–	30	20	75	2.50E-07	–	This study	–	
Busted Butte tuff	7.5–9	149 ± 10	–	4	1	150	–	1	Martin et al. (1997)	–	
Busted Butte tuff	7.5–9	141 ± 4	–	4	1	150	–	4	Martin et al. (1997)	–	
Busted Butte tuff	7.5–9	134.6	–	4	1	150	2.59E-06 ^a	250	Martin et al. (1997)	–	
Busted Butte tuff	7.5–9	134.2	–	4	1	150	–	636	Martin et al. (1997)	–	
Busted Butte tuff	7.5–9	132.8	–	4	1	150	1.44E-07 ^a	5848	Martin et al. (1997)	–	
Busted Butte tuff	7.5–9	127.8	–	4	1	150	–	1,960,000	Martin et al. (1997)	–	
Busted Butte tuff	7.5–9	131.4	–	4	1	150	–	–	Martin et al. (1997)	–	
Busted Butte tuff	7.5–9	131.3	–	4	1	150	–	–	Martin et al. (1997)	–	
Busted Butte tuff	7.5–9	115.0	–	4	1	150	–	–	Martin et al. (1997)	–	

Table 1 (continued)

Rock type	Porosity (%)	Differential stress (MPa)	σ_c/σ_p	Effective pressure (MPa)	Pore pressure (MPa)	T (°C)	Creep strain rate (/s)	Time-to-Failure (s)	Reference	Notes and additional information
Yucca Mountain tuff	11.3	70.0	–	10	0	225	–	–	Martin et al. (1997)	–
Yucca Mountain tuff	10.3	40.0	–	10	0	225	–	–	Martin et al. (1997)	–
Yucca Mountain tuff	9.2	129.0	–	10	0	225	–	–	Martin et al. (1997)	–
Yucca Mountain tuff	8.7	100.0	–	10	0	225	–	–	Martin et al. (1997)	–
Yucca Mountain tuff	11.4	98.0	–	10	0	225	–	–	Martin et al. (1997)	–
Yucca Mountain tuff	11.5	132.0	–	10	0	225	–	–	Martin et al. (1997)	–
Yucca Mountain tuff	8.8	131.0	–	10	0	225	–	–	Martin et al. (1997)	–
Tage tuff	20–30	5.9	0.900	10	0	RT	–	–	Okubo et al. (2008)	Transparent pressure vessel; time-lapse photography

^a Indicates that the value was calculated by the authors of this study.

^b Indicates that the value was taken from elsewhere in the literature.

therefore to use the stress corresponding to the onset of dilatancy dominance (D' in Fig. 2) as a *practical* lower limit for laboratory experiments. The choice of D' has two significant advantages; firstly, since it is a turning point, it is relatively easy to determine in real-time during an experiment (Heap et al., 2009a), and secondly, it yields experimental durations that are reasonable (from hours to weeks). The relationship between peak stress (σ_p), D' and C' is illustrated in Fig. 4 for Darley Dale sandstone over a range of effective mean stresses. We note that the relationships are linear and that the practical range of differential stress for laboratory creep experiments is about half of the expected theoretical range.

In practice, it has been found that for a given rock type and applied conditions (stress, effective pressure, temperature), creep strain rates can be highly variable from one sample to another. This variability is likely to be due to the intrinsic variability of rock microstructures (e.g., crack density, porosity). This problem of sample variability can be overcome, however, by employing a stress-stepping methodology that allows multiple measurements to be made using a single rock sample. In this methodology, the sample is first loaded to D' at a constant loading rate. The loading is then stopped and the sample allowed to deform through primary creep and into secondary creep at constant differential stress. When a sufficient level of secondary creep strain has been achieved to allow for accurate determination of the creep strain rate, the differential stress is stepped up by a small increment and the sample again allowed to deform until a further level of secondary creep strain allows the determination of a new, higher creep strain rate. This cycle is repeated until the sample fails. An illustration of this procedure on a sample of Darley Dale sandstone at an effective pressure of 30 MPa is given in Fig. 5. Note that brittle creep is never a *steady-state* process, since it is driven by irreversible crack growth. Hence, the microstructural state of samples evolves continuously throughout all creep experiments. The strain range between steps in stress-stepping experiments is extremely small (typically 0.01%), and the difference in sample microstructure between steps is therefore likely to also be very small, and much less than the difference in microstructure between two different samples. Indeed, for a range of different rocks, the comparison between results from stress-stepping tests and results from conventional creep tests shows that stress-stepping experiments provide more reliable creep strain rate data (Ngwenya et al., 2001; Heap et al., 2009a, 2011).

Since stress-stepping creep experiments eliminate sample variability, they are particularly useful for studying the influence of environmental conditions such as confining pressure, pore fluid pressure and temperature on the creep process. However, they are limited to quantifying secondary creep and provide only partial information about primary and tertiary creep. Hence, a full experimental programme to study brittle creep should involve a combination of both conventional and stress-stepping experiments.

3. Influence of environmental conditions on brittle creep in the laboratory

In this review we focus on triaxial creep experiments. Many studies conducted under uniaxial conditions have been reported, but we consider triaxial creep experiments to be more relevant to deformation in the Earth's crust. We gathered most of the published triaxial brittle creep data on rocks, which are presented in Table 1 (igneous and volcanic rocks) and Table 2 (sedimentary rocks). Note that some of the tabulated creep strain rates were not given in the original articles, and so were calculated directly from the published figures (all such data are indicated by ^a in Tables 1 and 2). In addition, we present some previously unpublished data to complement the existing dataset and to aid our discussion in the subsequent sections.

A brief survey of published data demonstrates that brittle creep has been observed in a wide variety of crustal rock types. Fig. 6 shows a set of creep curves (strain vs. time) for tests performed on granite, limestone, basalt and sandstone. Although the values of stress, confining pressure, strain and strain rate are different, the trimodal nature of the creep curves is essentially identical for all these major rock types. In the following sections, we use the available laboratory data to explain and discuss the systematic influence of stress (Section 3.1), pressure (Section 3.2), temperature (Section 3.3), fluid chemistry (Section 3.4), and microstructural state (Section 3.5) on brittle creep in crustal rocks.

3.1. The influence of differential stress

The majority of brittle creep studies have been focussed on the influence of the differential stress on the time-to-failure and/or the creep strain rate. A selection of these data, under similar pressure and temperature conditions, is presented in Figs. 7a and 8a. It can be seen, for all rock types tested, that time-to-failure and creep strain rate are strongly dependent on the level of the differential stress, illustrated by the need to use semi-log axes. In general, a small increase in differential stress results in a large increase in the creep strain rate, and an associated large decrease in the time-to-failure. For instance, for Inada granite (Fujii et al., 1999) at an effective pressure of 10 MPa, an increase in differential stress of only 4%, from 301 to 312 MPa, results in a decrease in time-to-failure, and an increase in creep strain rate by a factor of approximately 6. The strong effect of differential stress on time-to-failure and creep strain rate can be explained by the fact that an increase in the applied differential stress induces an increase in the stress intensity factor at microcrack tips within the rock. Even a modest increase in stress intensity factor results in a large increase in subcritical crack growth rate (e.g., Fig. 1). Hence, an increase in the applied differential stress on a bulk rock sample induces a large

Table 2
Summary of brittle creep data for sedimentary rocks under triaxial conditions.

Rock type	Porosity (%)	Differential stress (MPa)	σ_c/σ_p	Effective pressure (MPa)	Pore pressure (MPa)	T (°C)	Creep strain rate (/s)	Time-to-Failure (s)	Reference	Notes and additional information	
Gyda sandstone	4.3–20	84.3	–	6.9	13.8 (brine)	RT	6.53E–09	–	Ngwenya et al. (2001)	Creep exponents; microstructure	
Gyda sandstone	4.3–20	90.1	–	6.9	13.8 (brine)	RT	1.11E–08	–	Ngwenya et al. (2001)		
Gyda sandstone	4.3–20	95.9	–	6.9	13.8 (brine)	RT	1.56E–08	–	Ngwenya et al. (2001)		
Gyda sandstone	4.3–20	102.6	–	6.9	13.8 (brine)	RT	3.18E–08	–	Ngwenya et al. (2001)		
Gyda sandstone	4.3–20	109.2	–	6.9	13.8 (brine)	RT	5.00E–08	–	Ngwenya et al. (2001)		
Gyda sandstone	4.3–20	69.8	–	3.4	13.8 (brine)	RT	6.32E–09	–	Ngwenya et al. (2001)		
Gyda sandstone	4.3–20	75.2	–	3.4	13.8 (brine)	RT	7.39E–09	–	Ngwenya et al. (2001)		
Gyda sandstone	4.3–20	79.9	–	3.4	13.8 (brine)	RT	9.21E–09	–	Ngwenya et al. (2001)		
Gyda sandstone	4.3–20	85.7	–	3.4	13.8 (brine)	RT	2.27E–08	–	Ngwenya et al. (2001)		
Gyda sandstone	4.3–20	89.6	–	3.4	13.8 (brine)	RT	2.56E–08	–	Ngwenya et al. (2001)		
Gyda sandstone	4.3–20	93.0	–	13.8	13.8 (brine)	RT	3.84E–09	–	Ngwenya et al. (2001)		
Gyda sandstone	4.3–20	105.6	–	13.8	13.8 (brine)	RT	1.11E–08	–	Ngwenya et al. (2001)		
Gyda sandstone	4.3–20	99.5	–	13.8	13.8 (brine)	RT	1.10E–08	–	Ngwenya et al. (2001)		
Gyda sandstone	4.3–20	113.2	–	13.8	13.8 (brine)	RT	2.03E–08	–	Ngwenya et al. (2001)		
Gyda sandstone	4.3–20	119.5	–	13.8	13.8 (brine)	RT	3.26E–08	–	Ngwenya et al. (2001)		
Gyda sandstone	4.3–20	113.6	–	20.7	13.8 (brine)	RT	5.04E–09	–	Ngwenya et al. (2001)		
Gyda sandstone	4.3–20	99.2	–	20.7	13.8 (brine)	RT	1.46E–09	–	Ngwenya et al. (2001)		
Gyda sandstone	4.3–20	106.5	–	20.7	13.8 (brine)	RT	6.13E–09	–	Ngwenya et al. (2001)		
Gyda sandstone	4.3–20	121.6	–	20.7	13.8 (brine)	RT	9.63E–09	–	Ngwenya et al. (2001)		
Gyda sandstone	4.3–20	128.7	–	20.7	13.8 (brine)	RT	1.74E–08	–	Ngwenya et al. (2001)		
Magus sandstone	25.5–26.9	38.6	–	6.9	13.8 (brine)	RT	2.01E–08	–	Ngwenya et al. (2001)	Creep exponents; microstructure	
Magus sandstone	25.5–26.9	44.8	–	6.9	13.8 (brine)	RT	1.02E–07	–	Ngwenya et al. (2001)		
Magus sandstone	25.5–26.9	42.1	–	6.9	13.8 (brine)	RT	2.34E–08	–	Ngwenya et al. (2001)		
Magus sandstone	25.5–26.9	47.9	–	6.9	13.8 (brine)	RT	1.86E–07	–	Ngwenya et al. (2001)		
Magus sandstone	25.5–26.9	58.7	–	13.8	13.8 (brine)	RT	7.89E–08	–	Ngwenya et al. (2001)		
Magus sandstone	25.5–26.9	55.8	–	13.8	13.8 (brine)	RT	7.54E–08	–	Ngwenya et al. (2001)		
Magus sandstone	25.5–26.9	52.8	–	13.8	13.8 (brine)	RT	5.41E–08	–	Ngwenya et al. (2001)		
Magus sandstone	25.5–26.9	49.8	–	13.8	13.8 (brine)	RT	2.88E–08	–	Ngwenya et al. (2001)		
Magus sandstone	25.5–26.9	46.6	–	13.8	13.8 (brine)	RT	1.29E–08	–	Ngwenya et al. (2001)		
Magus sandstone	25.5–26.9	43.7	–	13.8	13.8 (brine)	RT	6.14E–09	–	Ngwenya et al. (2001)		
Magus sandstone	25.5–26.9	66.7	–	20.7	13.8 (brine)	RT	4.76E–08	–	Ngwenya et al. (2001)		
Magus sandstone	25.5–26.9	63.4	–	20.7	13.8 (brine)	RT	2.11E–08	–	Ngwenya et al. (2001)		
Magus sandstone	25.5–26.9	60.5	–	20.7	13.8 (brine)	RT	1.68E–08	–	Ngwenya et al. (2001)		
Magus sandstone	25.5–26.9	57.9	–	20.7	13.8 (brine)	RT	8.84E–09	–	Ngwenya et al. (2001)		
Magus sandstone	25.5–26.9	54.9	–	20.7	13.8 (brine)	RT	1.72E–09	–	Ngwenya et al. (2001)		
Magus sandstone	25.5–26.9	51.8	–	20.7	13.8 (brine)	RT	5.23E–10	–	Ngwenya et al. (2001)		
Gulfaks sandstone	20.9–34.7	6.6	–	6.9	13.8 (brine)	RT	9.98E–09	–	Ngwenya et al. (2001)		Creep exponents; microstructure
Gulfaks sandstone	20.9–34.7	8.3	–	6.9	13.8 (brine)	RT	1.08E–08	–	Ngwenya et al. (2001)		
Gulfaks sandstone	20.9–34.7	11.6	–	6.9	13.8 (brine)	RT	1.99E–08	–	Ngwenya et al. (2001)		
Gulfaks sandstone	20.9–34.7	15.0	–	6.9	13.8 (brine)	RT	2.45E–08	–	Ngwenya et al. (2001)		
Gulfaks sandstone	20.9–34.7	19.8	–	13.8	13.8 (brine)	RT	1.18E–07	–	Ngwenya et al. (2001)		
Gulfaks sandstone	20.9–34.7	18.1	–	13.8	13.8 (brine)	RT	1.58E–07	–	Ngwenya et al. (2001)		
Gulfaks sandstone	20.9–34.7	16.5	–	13.8	13.8 (brine)	RT	2.43E–07	–	Ngwenya et al. (2001)		
Gulfaks sandstone	20.9–34.7	13.1	–	13.8	13.8 (brine)	RT	5.88E–07	–	Ngwenya et al. (2001)		
Gulfaks sandstone	20.9–34.7	29.7	–	27.6	13.8 (brine)	RT	1.48E–07	–	Ngwenya et al. (2001)		
Gulfaks sandstone	20.9–34.7	26.3	–	27.6	13.8 (brine)	RT	1.34E–07	–	Ngwenya et al. (2001)		
Gulfaks sandstone	20.9–34.7	23.0	–	27.6	13.8 (brine)	RT	2.41E–07	–	Ngwenya et al. (2001)		
Gulfaks sandstone	20.9–34.7	19.5	–	27.6	13.8 (brine)	RT	4.10E–07	–	Ngwenya et al. (2001)		
Darley Dale sandstone	14.26	130.0	0.80	30	45	RT	3.00E–09	1200	Baud and Meredith (1997)	AE; volumetric strain	
Darley Dale sandstone	14.35	138.0	0.85	30	45	RT	8.00E–08	290	Baud and Meredith (1997)		
Darley Dale sandstone	12.75	146.0	0.90	30	45	RT	7.00E–07	67	Baud and Meredith (1997)		
Bentheim sandstone	23.41	120.3	0.86	30	20	RT	4.56E–09	–	Heap et al. (2009b)		
Bentheim sandstone	23.41	122.3	0.87	30	20	RT	1.14E–08	–	Heap et al. (2009b)		
Bentheim sandstone	23.41	123.8	0.88	30	20	RT	3.00E–08	–	Heap et al. (2009b)		
Bentheim sandstone	23.41	126.4	0.90	30	20	RT	1.01E–07	–	Heap et al. (2009b)		
Bentheim sandstone	23.41	130.1	0.93	30	20	RT	5.67E–07	–	Heap et al. (2009b)		
Bentheim sandstone	23.38	97.7	0.74	30	20	75	1.19E–07	–	Heap et al. (2009b)		
Bentheim sandstone	23.38	90.3	0.68	30	20	75	2.09E–08	–	Heap et al. (2009b)		
Bentheim sandstone	23.38	104.1	0.79	30	20	75	3.50E–07	–	Heap et al. (2009b)		
Bentheim sandstone	23.38	109.1	0.83	30	20	75	9.00E–07	–	Heap et al. (2009b)		
Crab Orchard sandstone	3.27	376.4	0.93	30	20	RT	1.29E–08	–	Heap et al. (2009b)		
Crab Orchard sandstone	3.27	382.0	0.94	30	20	RT	3.67E–08	–	Heap et al. (2009b)		
Crab Orchard sandstone	3.27	390.9	0.97	30	20	RT	2.00E–07	–	Heap et al. (2009b)		
Crab Orchard sandstone	3.27	385.5	0.95	30	20	RT	1.00E–07	–	Heap et al. (2009b)		
Crab Orchard sandstone	3.32	363.2	0.92	30	20	75	1.12E–07	–	Heap et al. (2009b)		
Crab Orchard sandstone	3.32	366.9	0.93	30	20	75	2.24E–07	–	Heap et al. (2009b)		
Crab Orchard sandstone	3.32	370.6	0.94	30	20	75	3.49E–07	–	Heap et al. (2009b)		
Crab Orchard sandstone	3.32	373.5	0.95	30	20	75	5.50E–07	–	Heap et al. (2009b)		
Darley Dale sandstone	13.33	124.1	0.80	30	20	RT	2.00E–09	–	Heap et al. (2009a)	AE; volumetric strain; AE locations; power law model; microstructure	
Darley Dale sandstone	13.33	128.2	0.83	30	20	RT	6.00E–09	–	Heap et al. (2009a)		
Darley Dale sandstone	13.33	134.1	0.87	30	20	RT	6.90E–08	–	Heap et al. (2009a)		
Darley Dale sandstone	13.33	140.6	0.91	30	20	RT	5.50E–07	–	Heap et al. (2009a)		

Table 2 (continued)

Rock type	Porosity (%)	Differential stress (MPa)	σ_c/σ_p	Effective pressure (MPa)	Pore pressure (MPa)	T (°C)	Creep strain rate (/s)	Time-to-Failure (s)	Reference	Notes and additional information
Darley Dale sandstone	13.33	143.3	0.92	30	20	RT	1.20E–06	–	Heap et al. (2009a)	
Darley Dale sandstone	13.31	111.5	–	30	20	45	2.00E–08	–	Heap et al. (2009a)	
Darley Dale sandstone	13.31	115.7	–	30	20	45	6.52E–08	–	Heap et al. (2009a)	
Darley Dale sandstone	13.31	122.5	–	30	20	45	2.40E–07	–	Heap et al. (2009a)	
Darley Dale sandstone	13.31	133.4	–	30	20	45	2.40E–06	–	Heap et al. (2009a)	
Darley Dale sandstone	13.31	129.7	–	30	20	45	7.00E–07	–	Heap et al. (2009a)	
Darley Dale sandstone	13.3	103.4	0.73	30	20	75	4.66E–08	–	Heap et al. (2009a)	
Darley Dale sandstone	13.3	107.4	0.76	30	20	75	1.14E–07	–	Heap et al. (2009a)	
Darley Dale sandstone	13.3	111.3	0.78	30	20	75	2.31E–07	–	Heap et al. (2009a)	
Darley Dale sandstone	13.3	115.5	0.81	30	20	75	3.62E–07	–	Heap et al. (2009a)	
Darley Dale sandstone	13.3	119.8	0.84	30	20	75	7.85E–07	–	Heap et al. (2009a)	
Darley Dale sandstone	13.3	123.1	0.87	30	20	75	1.50E–06	–	Heap et al. (2009a)	
Darley Dale sandstone	13.29	71.8	0.68	10	20	RT	1.30E–09	–	Heap et al. (2009a)	
Darley Dale sandstone	13.29	73.2	0.70	10	20	RT	3.00E–09	–	Heap et al. (2009a)	
Darley Dale sandstone	13.29	73.8	0.70	10	20	RT	6.50E–09	–	Heap et al. (2009a)	
Darley Dale sandstone	13.29	75.8	0.72	10	20	RT	3.52E–08	–	Heap et al. (2009a)	
Darley Dale sandstone	13.29	80.2	0.76	10	20	RT	4.00E–07	–	Heap et al. (2009a)	
Darley Dale sandstone	13.31	164.6	0.89	50	20	RT	1.03E–08	–	Heap et al. (2009a)	
Darley Dale sandstone	13.31	168.0	0.91	50	20	RT	1.76E–08	–	Heap et al. (2009a)	
Darley Dale sandstone	13.31	171.3	0.93	50	20	RT	2.47E–08	–	Heap et al. (2009a)	
Darley Dale sandstone	13.31	177.1	0.96	50	20	RT	1.63E–07	–	Heap et al. (2009a)	
Darley Dale sandstone	13.31	185.5	1.00	50	20	RT	7.00E–07	–	Heap et al. (2009a)	
Darley Dale sandstone	13.31	191.0	1.03	50	20	RT	2.18E–06	–	Heap et al. (2009a)	
Darley Dale sandstone	13.3	132.3	0.85	50	40	RT	6.71E–09	–	Heap et al. (2009a)	
Darley Dale sandstone	13.3	135.7	0.88	50	40	RT	1.91E–08	–	Heap et al. (2009a)	
Darley Dale sandstone	13.3	140.0	0.90	50	40	RT	1.10E–07	–	Heap et al. (2009a)	
Darley Dale sandstone	13.3	145.0	0.94	50	40	RT	5.03E–07	–	Heap et al. (2009a)	
Darley Dale sandstone	13.3	147.5	0.95	50	40	RT	8.00E–07	–	Heap et al. (2009a)	
Darley Dale sandstone	13.35	141.3	0.91	30	20	RT	3.58E–06	600	Heap et al. (2009a)	
Darley Dale sandstone	13.32	132.6	0.86	30	20	RT	1.79E–07	9600	Heap et al. (2009a)	
Darley Dale sandstone	13.32	125.0	0.81	30	20	RT	1.32E–08	216,000	Heap et al. (2009a)	
Darley Dale sandstone	13.33	122.0	0.79	30	20	RT	3.77E–09	777,600	Heap et al. (2009a)	
Darley Dale sandstone	13.28	118.8	0.77	30	20	RT	2.12E–09	–	Heap et al. (2009a)	
Darley Dale sandstone	13.8	87.4	0.97	10	10	RT	1.28E–07	13,680	This study	D' = 75.80 MPa
Darley Dale sandstone	13.5	81.0	0.90	10	10	RT	1.44E–09	1,612,860	This study	D' = 72.50 MPa
Darley Dale sandstone	13.9	84.0	0.93	10	10	RT	4.38E–07	4800	This study	D' = 71.10 MPa
Darley Dale sandstone	13.8	83.3	0.93	10	10	RT	3.30E–08	61,680	This study	D' = 72.00 MPa
Darley Dale sandstone	14	80.0	0.89	10	10	RT	1.25E–08	194,400	This study	D' = 71.11 MPa
Darley Dale sandstone	14.4	82.5	0.92	10	10	RT	1.30E–07	15,240	This study	D' = 72.22 MPa
Darley Dale sandstone	14.9	79.5	0.88	10	10	RT	1.48E–08	87,600	This study	D' = 70.90 MPa
Darley Dale sandstone	14.1	82.6	0.92	10	10	RT	3.20E–08	62,400	This study	D' = 73.33 MPa
Darley Dale sandstone	14	78.6	0.87	10	10	RT	1.62E–09	1,430,760	This study	D' = 74.22 MPa
Darley Dale sandstone	14.1	84.0	0.93	10	10	RT	1.63E–07	13,380	This study	D' = 71.67 MPa
Darley Dale sandstone	14.3	80.4	0.89	10	10	RT	5.19E–09	108,480	This study	D' = 75.00 MPa
Darley Dale sandstone	14.65	85.1	0.95	10	10	RT	1.72E–07	12,060	This study	D' = 73.88 MPa
Mushan sandstone	14.1	–	0.76	20	0	RT	6.92E–08 ^a	–	Tsai et al. (2008)	Volumetric strain;
Mushan sandstone	14.1	–	0.86	20	0	RT	1.05E–07 ^a	–	Tsai et al. (2008)	viscoelastic model
Mushan sandstone	14.1	–	0.91	20	0	RT	1.57E–07 ^a	–	Tsai et al. (2008)	
Xiangjiaba sandstone	–	160.0	0.89	5	0	RT	3.28E–09 ^a	111,024	Yang and Jiang (2010)	Macroscopic
Xiangjiaba sandstone/coal	–	150.0	–	5	0	RT	2.90E–09 ^a	103,716	Yang and Jiang (2010)	fracture analysis
Thala limestone	17.5	95.0	0.88	20	10	RT	5.40E–07	5044	This study	–
Tavel limestone	6.43	153.0	0.71	30	20	RT	2.30E–08	–	This study	–
Tavel limestone	6.43	163.3	0.76	30	20	RT	8.17E–08	–	This study	–
Tavel limestone	6.43	167.3	0.78	30	20	RT	2.12E–07	–	This study	–
Tavel limestone	6.43	171.3	0.80	30	20	RT	1.24E–06	–	This study	–
Tavel limestone	6.43	175.3	0.82	30	20	RT	4.52E–06	–	This study	–
Turonian oolitic limestone	23	12.5	0.51	5	0	RT	No steady-rate creep	–	Xie et al. (2011)	Radial strain; permeability
Turonian oolitic limestone (chemically degraded)	27	12.5	0.57	5	0.1	RT	No steady-rate creep	–	Xie et al. (2011)	
Lavoux limestone	24.5	15.0	0.33	15	10 (CO2)	70	3.98E–10 ^a (steady-rate?)	–	Grgic (2011)	CO2 injection
Bure clay (5697)	–	10.0	–	12	0 (wet)	RT	4.46E–11	–	Gasc-Barbier et al. (2004)	–
Bure clay (5697)	–	0.0	–	12	0 (wet)	80	–1.91E–11	–	Gasc-Barbier et al. (2004)	–
Bure clay (5697)	–	15.0	–	12	0 (wet)	80	3.50E–10	–	Gasc-Barbier et al. (2004)	–
Bure clay (5697)	–	0.0	–	12	0 (wet)	RT	1.21E–11	–	Gasc-Barbier et al. (2004)	–
Bure clay (5697)	–	10.0	–	12	0 (wet)	RT	1.97E–11	–	Gasc-Barbier et al. (2004)	–
Bure clay (5697)	–	10.0	–	12	0 (wet)	RT	4.71E–11	–	Gasc-Barbier et al. (2004)	–
Bure clay (5697)	–	15.0	–	12	0 (wet)	RT	2.01E–10	–	Gasc-Barbier et al. (2004)	–
Bure clay (5697)	–	0.0	–	12	0 (wet)	RT	–2.03E–11	–	Gasc-Barbier et al. (2004)	–

(continued on next page)

Table 2 (continued)

Rock type	Porosity (%)	Differential stress (MPa)	σ_c/σ_p	Effective pressure (MPa)	Pore pressure (MPa)	T (°C)	Creep strain rate (/s)	Time-to-Failure (s)	Reference	Notes and additional information
Bure clay (5697)	–	2.0	–	12	0 (wet)	RT	1.21E–11	–	Gasc-Barbier et al. (2004)	
Bure clay (5697)	–	5.0	–	12	0 (wet)	RT	9.82E–11	–	Gasc-Barbier et al. (2004)	
Bure clay (5697)	–	10.0	–	12	0 (wet)	RT	2.01E–10	–	Gasc-Barbier et al. (2004)	
Bure clay (5697)	–	0.0	–	12	0 (wet)	RT	–4.03E–11	–	Gasc-Barbier et al. (2004)	
Bure clay (5697)	–	15.0	–	12	0 (wet)	RT	7.84E–11	–	Gasc-Barbier et al. (2004)	
Bure clay (5698)	–	0.0	–	12	0 (wet)	80	–2.28E–11	–	Gasc-Barbier et al. (2004)	
Bure clay (5698)	–	2.0	–	12	0 (wet)	80	5.58E–11	–	Gasc-Barbier et al. (2004)	
Bure clay (5698)	–	5.0	–	12	0 (wet)	80	6.70E–11	–	Gasc-Barbier et al. (2004)	
Bure clay (5698)	–	10.0	–	12	0 (wet)	80	2.28E–10	–	Gasc-Barbier et al. (2004)	
Bure clay (5698)	–	0.0	–	12	0 (wet)	RT	–1.01E–10	–	Gasc-Barbier et al. (2004)	
Bure clay (5698)	–	10.0	–	12	0 (wet)	RT	9.83E–11	–	Gasc-Barbier et al. (2004)	
Bure clay (5698)	–	15.0	–	12	0 (wet)	RT	9.83E–11	–	Gasc-Barbier et al. (2004)	
Bure clay (5698)	–	17.0	–	12	0 (wet)	RT	1.99E–10	–	Gasc-Barbier et al. (2004)	
Sioux quartzite	–	594.0	–	200	0	480	3.84E–10 ^a	–	Ross et al. (1983)	Microcrack orientation analysis
Sioux quartzite	–	594.0	–	200	0	570	6.14E–10 ^a	–	Ross et al. (1983)	
Sioux quartzite	–	594.0	–	200	0	600	1.39E–09 ^a	–	Ross et al. (1983)	
Sioux quartzite	–	594.0	–	200	0	634	4.78E–10 ^a	–	Ross et al. (1983)	
Sioux quartzite	–	594.0	–	200	0	660	3.12E–09 ^a	–	Ross et al. (1983)	
Sioux quartzite	–	594.0	–	200	0	720	5.88E–09 ^a	–	Ross et al. (1983)	
Sioux quartzite	–	594.0	–	200	0	730	8.01E–09 ^a	–	Ross et al. (1983)	
Sioux quartzite	–	594.0	–	200	0	769	5.91E–08 ^a	–	Ross et al. (1983)	
Felser sandstone	20.4	30.9	–	14.9	2.8	150	1.10E–09	–	Hettema et al. (1991)	
Felser sandstone	20.4	46.7	–	15.0	2.9	150	1.20E–09	–	Hettema et al. (1991)	
Felser sandstone	20.4	38.6	–	15.0	4.1	200	No steady-rate creep	–	Hettema et al. (1991)	
Felser sandstone	20.4	46.4	–	15.0	3.1	200	1.20E–09	–	Hettema et al. (1991)	
Felser sandstone	20.4	54.5	–	15.0	3.0	200	1.70E–09	–	Hettema et al. (1991)	
Felser sandstone	20.4	54.7	–	15.0	5.4	16	No steady-rate creep	–	Hettema et al. (1991)	
Felser sandstone	20.4	38.9	–	15.1	5.1	250	8.00E–10	–	Hettema et al. (1991)	
Felser sandstone	20.4	46.5	–	15.0	5.2	250	1.00E–09	–	Hettema et al. (1991)	
Felser sandstone	20.4	54.6	–	15.0	5.2	250	No steady-rate creep	–	Hettema et al. (1991)	
Beringen siltstone	1.5	54.3	–	15.0	4.9	250	4.20E–10	–	Hettema et al. (1991)	Microstructure
Beringen siltstone	1.5	54.5	–	15.0	0	600	No steady-rate creep	–	Hettema et al. (1991)	
Beringen siltstone	1.5	54.3	–	15.0	0	800	2.3E–09 or 1.0E–09	–	Hettema et al. (1991)	
Beringen siltstone	1.5	48.3	–	15.0	0	500	5.00E–10	–	Hettema et al. (1991)	
Beringen siltstone	1.5	56.4	–	15.0	0	500	1.10E–09	–	Hettema et al. (1991)	
Beringen siltstone	1.5	64.4	–	15.0	0	500	7.00E–10	–	Hettema et al. (1991)	
Beringen siltstone	1.5	65.5	–	15.0	0	600	No steady-rate creep	–	Hettema et al. (1991)	
Beringen siltstone	1.5	65.5	–	15.0	0	700	No steady-rate creep	–	Hettema et al. (1991)	
Beringen siltstone	1.5	65.5	–	15.0	0	800	3.8E–09 or 1.8E–09	–	Hettema et al. (1991)	
Beringen siltstone	1.5	65.4	–	15.0	0	900	No steady-rate creep	–	Hettema et al. (1991)	
Opohonga dolomitized limestone	3.45	2.8	0.02	3.8	0 (wet)	RT	–	–	Cogan (1976)	Volumetric strain
Opohonga dolomitized limestone	3.45	7.8	0.07	3.8	0 (wet)	RT	1.40E–10	–	Cogan (1976)	
Opohonga dolomitized limestone	3.45	15.5	0.13	3.8	0 (wet)	RT	2.05E–10	–	Cogan (1976)	
Opohonga dolomitized limestone	3.45	27.4	0.53	3.8	0 (wet)	RT	–	–	Cogan (1976)	
Opohonga dolomitized limestone	3.45	0.8	0.01	0.3	0 (wet)	RT	1.04E–08	–	Cogan (1976)	
Opohonga dolomitized limestone	3.45	1.9	0.01	0.3	0 (wet)	RT	1.30E–08	–	Cogan (1976)	
Opohonga dolomitized limestone	3.45	7.9	0.06	0.3	0 (wet)	RT	1.41E–03	–	Cogan (1976)	
Opohonga dolomitized limestone	3.45	16.9	0.11	0.3	0 (wet)	RT	2.89E–03	–	Cogan (1976)	
Ophir hard shale	11	1.0	0.04	0.3	0 (wet)	RT	3.85E–09	–	Cogan (1976)	
Ophir hard shale	11	1.2	0.04	0.4	0 (wet)	RT	5.14E–09	–	Cogan (1976)	
Ophir hard shale	11	2.5	0.09	0.4	0 (wet)	RT	1.20E–08	–	Cogan (1976)	
Ophir hard shale	11	6.4	0.22	0.4	0 (wet)	RT	4.95E–09	–	Cogan (1976)	
Ophir hard shale	11	7.8	0.27	1.4	0 (wet)	RT	5.07E–09	–	Cogan (1976)	
Ophir hard shale	11	1.7	0.03	3.4	0 (wet)	RT	7.26E–09	–	Cogan (1976)	
Ophir hard shale	11	6.2	0.12	3.4	0 (wet)	RT	1.60E–08	–	Cogan (1976)	
Ophir hard shale	11	29.6	0.56	3.4	0 (wet)	RT	1.25E–08	–	Cogan (1976)	

Table 2 (continued)

Rock type	Porosity (%)	Differential stress (MPa)	σ_c/σ_p	Effective pressure (MPa)	Pore pressure (MPa)	T (°C)	Creep strain rate (/s)	Time-to-Failure (s)	Reference	Notes and additional information
Ophir limey shale	13	0.6	0.06	0.3	0 (wet)	RT	6.17E–09	–	Cogan (1976)	Volumetric strain
Ophir limey shale	13	1.6	0.11	0.3	0 (wet)	RT	4.20E–09	–	Cogan (1976)	
Ophir limey shale	13	3.8	0.28	0.3	0 (wet)	RT	3.58E–09	–	Cogan (1976)	
Ophir limey shale	13	6.6	0.48	0.3	0 (wet)	RT	1.22E–08	–	Cogan (1976)	
Ophir limey shale	13	1.3	0.11	1.2	0 (wet)	RT	1.02E–08	–	Cogan (1976)	
Ophir limey shale	13	2.0	0.18	1.3	0 (wet)	RT	2.14E–09	–	Cogan (1976)	
Ophir limey shale	13	4.7	0.41	1.3	0 (wet)	RT	4.65E–09	–	Cogan (1976)	
Ophir soft shale	7	1.0	0.45	1.4	0 (wet)	RT	1.98E–04	–	Cogan (1976)	
Ophir soft shale	7	1.5	0.64	1.4	0 (wet)	RT	3.29E–04	–	Cogan (1976)	
Ophir soft shale	7	2.1	0.89	1.4	0 (wet)	RT	7.24E–04	–	Cogan (1976)	
Xiangjiaba sandstone (weathered)	–	2.5	–	1	0	RT	6.51E–09	–	Zhang et al. (2012)	Radial strain; volumetric strain
Xiangjiaba sandstone (weathered)	–	3.3	–	1	0	RT	7.04E–09	–	Zhang et al. (2012)	
Xiangjiaba sandstone (weathered)	–	3.9	–	1	0	RT	8.79E–09	–	Zhang et al. (2012)	
Xiangjiaba sandstone (weathered)	–	4.4	–	1	0	RT	1.38E–08	–	Zhang et al. (2012)	
Xiangjiaba sandstone (weathered)	–	2.8	–	1.5	0	RT	2.59E–09	–	Zhang et al. (2012)	
Xiangjiaba sandstone (weathered)	–	3.4	–	1.5	0	RT	2.42E–09	–	Zhang et al. (2012)	
Xiangjiaba sandstone (weathered)	–	4.0	–	1.5	0	RT	2.33E–09	–	Zhang et al. (2012)	
Xiangjiaba sandstone (weathered)	–	4.6	–	1.5	0	RT	3.88E–09	–	Zhang et al. (2012)	
Xiangjiaba sandstone (weathered)	–	5.2	–	1.5	0	RT	3.97E–09	–	Zhang et al. (2012)	
Xiangjiaba sandstone (weathered)	–	6.0	–	1.5	0	RT	4.07E–09	–	Zhang et al. (2012)	
Xiangjiaba sandstone (weathered)	–	6.8	–	1.5	0	RT	6.30E–09	–	Zhang et al. (2012)	
Xiangjiaba sandstone (weathered)	–	7.6	–	1.5	0	RT	5.62E–09	–	Zhang et al. (2012)	
Xiangjiaba sandstone (weathered)	–	3.0	–	2	0	RT	2.16E–09	–	Zhang et al. (2012)	
Xiangjiaba sandstone (weathered)	–	3.8	–	2	0	RT	2.14E–09	–	Zhang et al. (2012)	
Xiangjiaba sandstone (weathered)	–	4.8	–	2	0	RT	2.44E–09	–	Zhang et al. (2012)	
Xiangjiaba sandstone (weathered)	–	5.8	–	2	0	RT	3.18E–09	–	Zhang et al. (2012)	
Xiangjiaba sandstone (weathered)	–	6.8	–	2	0	RT	3.69E–09	–	Zhang et al. (2012)	
Xiangjiaba sandstone (weathered)	–	7.8	–	2	0	RT	4.27E–09	–	Zhang et al. (2012)	
Xiangjiaba sandstone (weathered)	–	8.8	–	2	0	RT	4.20E–09	–	Zhang et al. (2012)	
Xiangjiaba sandstone (weathered)	–	9.8	–	2	0	RT	7.40E–09	–	Zhang et al. (2012)	
Pietra Leccese limestone	38	30.0	0.83	15	0	RT	5.35E–10 ^a (steady-rate?)	–	Maranini and Brignoli (1999)	Elastic moduli; hydrostatic creep tests; volumetric strain
Pietra Leccese limestone	38	25.0	0.69	15	0	RT	3.56E–10 ^a (steady-rate?)	–	Maranini and Brignoli (1999)	
Pietra Leccese limestone	38	20.0	0.56	15	0	RT	2.83E–10 ^a (steady-rate?)	–	Maranini and Brignoli (1999)	
Pietra Leccese limestone	38	40.0	1.18	30	0	RT	8.68E–11 ^a (steady-rate?)	–	Maranini and Brignoli (1999)	
Pietra Leccese limestone	38	30.0	0.88	30	0	RT	1.65E–10 ^a (steady-rate?)	–	Maranini and Brignoli (1999)	
Pietra Leccese limestone	38	20.0	0.59	30	0	RT	5.16E–11 ^a (steady-rate?)	–	Maranini and Brignoli (1999)	

^a Indicates that the value was calculated by the authors of this study.

increase in the macroscopic creep strain rate, and a large decrease in the time-to-failure.

When comparing times-to-failure or creep strain rates between various rocks as a function of applied differential stress, we have to bear in mind that the stress range over which brittle creep occurs, i.e., from the onset of cracking (C') to the short-term strength (σ_p), will vary significantly and depend on the rock type. Therefore, in order to make meaningful comparisons between rock types, it is

desirable to normalise the creep stresses within their upper and lower bounds. The theoretical upper bound is the peak stress at a strain rate that is sufficiently high for the deformation to be essentially time-independent. However, since samples are generally pre-loaded to their creep stress at strain rates close to 10^{-5} s^{-1} , we have used the peak stress from constant strain rate tests at that strain rate as the practical reference upper bound. The lower bound is simply the lowest stress at which crack growth is possible.

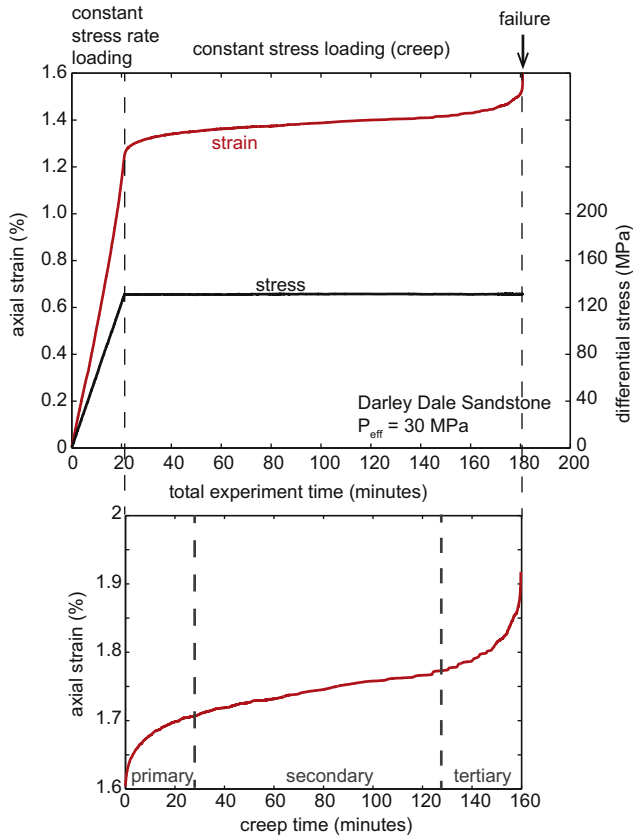


Fig. 3. Strain–time and stress–time plot for a conventional creep experiment on a sample of Darley Dale sandstone illustrating the experimental protocol. The experiment is divided into two phases: an initial constant stress rate loading phase and a constant stress (creep) phase. The inset shows a zoomed-in view of the constant stress phase. The three creep phases (primary, secondary, and tertiary) are labelled on the inset. Data from Heap et al., 2009a.

However, the lower bound for the onset of cracking (C') in constant strain rate experiments should be affected by stress corrosion and hence be time-dependent, so that the C' obtained at any arbitrary strain rate does not necessarily reflect the lowest possible creep stress. However, considering that (1) brittle creep eventually results in sliding on a fault, and (2) crack initiation occurs at the tips of

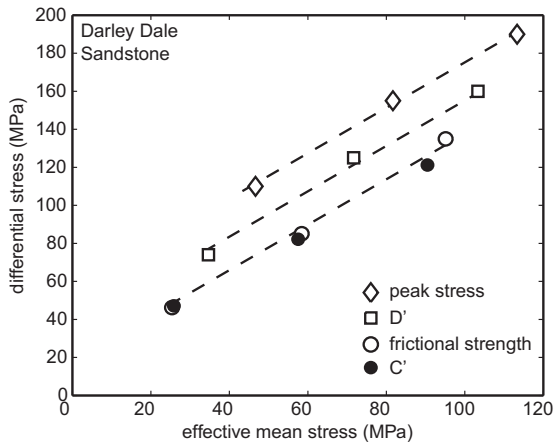


Fig. 4. Effective mean stress–differential stress diagram showing experimentally-derived (from constant strain rate (10^{-5} s^{-1}) experiments) values for the short-term peak stress (diamonds), D' (squares), and σ_F (circles) at effective pressures of 10, 30, and 50 MPa. Redrawn after Heap et al., 2009a.

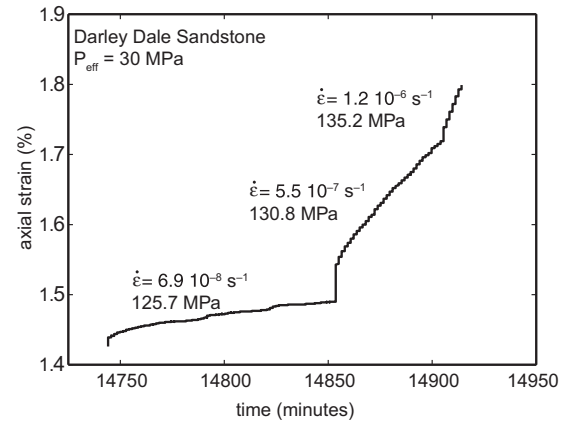


Fig. 5. Strain–time diagram taken from a segment of a stress-stepping creep experiment on Darley Dale sandstone to demonstrate the stress-stepping methodology. The figure shows the stress steps and the intervals over which the creep strain rates were calculated. The sample in this experiment failed after about 14920 min, about 10.4 days. Redrawn after Heap et al., 2009a.

sliding defects (e.g., Ashby and Hallam, 1986; Ashby and Sammis, 1990), the frictional stress provides a conservative estimate for the lower bound of the creep stress. Theoretical justification for this can be found by analysing the expression for the stress at the onset of crack growth at the tips of favourably oriented sliding defects, as given by Ashby and Hallam (1986):

$$\sigma_1 = \frac{\sqrt{1 + \mu^2} + \mu}{\sqrt{1 + \mu^2} - \mu} \sigma_3 + \frac{\sqrt{3}}{\sqrt{1 + \mu^2} - \mu} \frac{K_{IC}}{\sqrt{\pi a}}, \quad (6)$$

where σ_1 and σ_3 are the maximum and minimum principal stresses, respectively, μ is the friction coefficient on the flaw, and a is the half-length of the flaw. Expression (6) has thus the form of a frictional term plus a cohesion term, and is valid if K_{IC} is the crack growth criterion. Because of stress corrosion, crack growth is possible for $K_I < K_{IC}$, and using $K_I = 0$ provides a global lower bound for the stress. This effectively implies that friction is the limiting factor in the level of stress at the onset of cracking. Indeed, it is generally observed empirically that C' is very close to the residual friction (Paterson and Wong, 2005; see also Fig. 4). Hence, we use a normalised stress, σ^* , defined as:

$$\sigma^* = \frac{\sigma_C - \sigma_F}{\sigma_P - \sigma_F}, \quad (7)$$

where σ_C is the applied creep differential stress, σ_F is the frictional strength, and σ_P is the short-term strength. This normalised stress ranges from 0 at $\sigma_C = \sigma_F$ (our assumed theoretical lower stress limit for creep) to 1 at $\sigma_C = \sigma_P$ (when the creep stress is equal to the short-term strength, and therefore the time-to-failure should tend to zero). When frictional strengths were not directly available, they were estimated using Coulomb's criterion with a friction coefficient of 0.5 (well within Byerlee's estimates at low confining pressures). Plots of times-to-failure and creep strain rates as a function of the normalised stress are shown in Figs. 7b and 8b.

We note that the times-to-failure plotted as a function of σ^* (Fig. 7b) all converge to a similar value as the normalised stress approaches 1. The differences in the slopes of the curves are not only due to variations in the creep strain rates, but also due to variations in the total amount of strain that can be accumulated in the rock before failure (e.g., high-porosity sandstones require more strain to reach failure than low-porosity granites). For this reason, the most meaningful direct comparisons of the curves for the different rock types can be made using the creep strain rate curves.

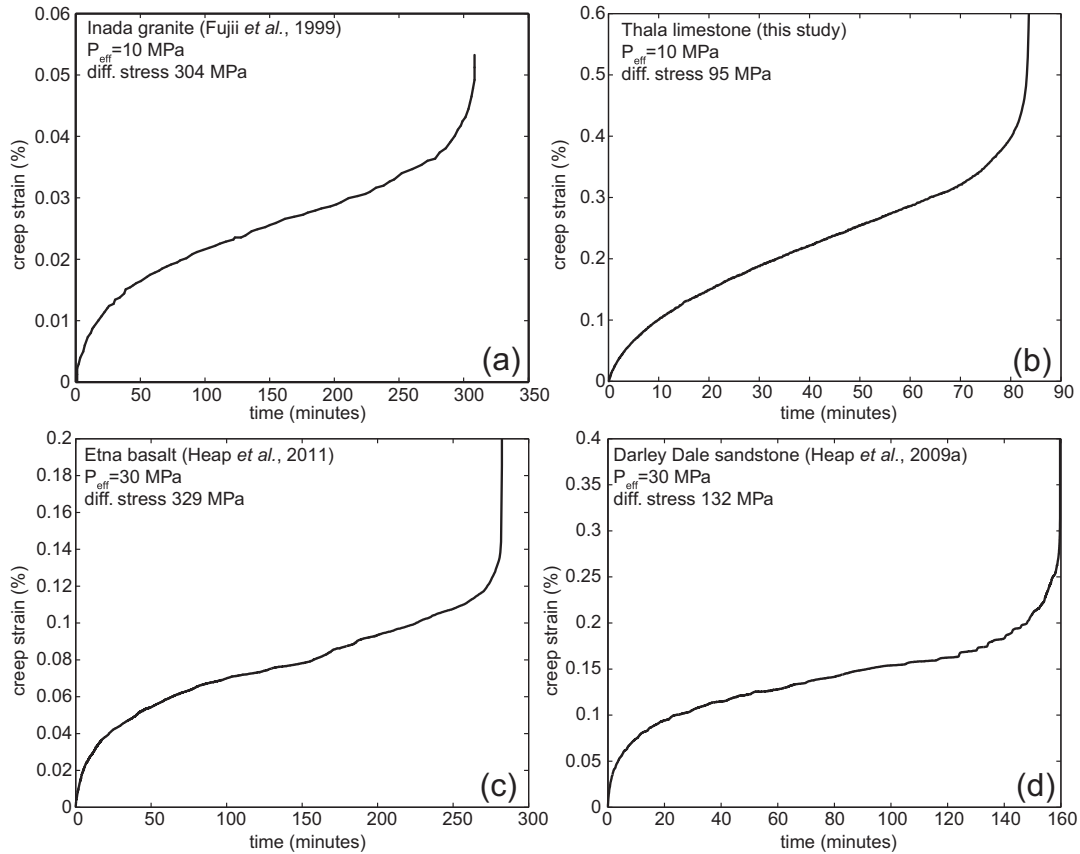


Fig. 6. Strain–time or “creep curves” for Inada granite (Fujii et al., 1999), Thala limestone (this study), Etna basalt (Heap et al., 2011), and Darley Dale sandstone (Heap et al., 2009a) from conventional creep experiments under triaxial pressure conditions. The effective pressure (P_{eff}) and the creep differential stress are indicated on each graph.

In general, it could be said that the stress sensitivity of the time-to-failure and creep strain rate to the differential stress (i.e., the gradients of the curves) is greater for sandstones than for igneous rocks (Figs. 7b and 8b). Perhaps this is not surprising since single crack experiments have shown that subcritical tensile crack growth is much faster in quartz (at the same level of stress) than in any other material (Atkinson, 1984). In Fig. 8b, we observe some differences in the normalised stress required to achieve a given creep strain rate for different rock types. In particular, the rocks for which we see the greatest differences are Tavel limestone (a micritic limestone with a porosity of about 10%) and Crab Orchard sandstone (a quartz-rich, highly cemented, sandstone with a porosity of about 4%). In the strain rate range 10^{-8} – 10^{-6} s^{-1} , Tavel limestone undergoes creep at significantly lower normalised stresses ($\sigma^* \approx 0.6$) compared to Crab Orchard sandstone ($\sigma^* \approx 0.9$). This difference might be due to the fact that subcritical crack growth is already fast at low stress intensity factors (i.e., at low overall differential stress) in calcite, whereas it requires K_I to be close to K_{IC} (i.e., the differential stress must be closer to the peak stress) in quartz (e.g., Atkinson, 1984). Indeed, microplasticity and dissolution, in addition to stress corrosion, have been invoked as potentially important mechanisms of subcritical crack growth in calcite (Atkinson, 1984; Røyne et al. 2011).

3.2. The influence of effective pressure

The influence of effective pressure on the time-to-failure and creep strain rate is illustrated in the log-linear plots of Figs. 9a and 10a, respectively. The data show that effective pressure has a profound influence on times-to-failure and creep strain rates, for all

of the rock types tested. The time-to-failure (Fig. 9) and creep strain rate (Fig. 10) curves are shifted to higher values of differential stress as the effective pressure is increased. For the example of Barre granite (Fig. 9), if we take a single value of differential stress (say, 500 MPa) and extrapolate the data for the $P_{\text{eff}} = 53$ and 101 MPa curves, the time-to-failure increases by about 8 orders of magnitude at the higher effective pressure. Similarly, for Darley Dale sandstone (Fig. 10), the creep strain rate at a differential stress of 150 MPa is reduced by about 5 orders of magnitude when the effective pressure is increased from 30 to 50 MPa.

A decrease in strain rate (and, accordingly, an increase in time-to-failure) in response to an increase in effective pressure is to be expected, as we know that rock strength increases at higher effective pressure (Paterson and Wong, 2005). However, while the increase in short-term strength (as observed in fast constant strain rate experiments) scales approximately linearly with the increase in effective pressure (e.g., the strength of Darley Dale sandstone increases by 20% from $P_{\text{eff}} = 30$ to 50 MPa), the creep strain rate taken at a given differential stress is non-linear, and decreases by many orders of magnitude as effective pressure is increased. This non-linearity can be explained by the extreme sensitivity of the microcrack growth rate to the local stress intensity factor (e.g., according to Eq. (4); see Fig. 1): Increasing the effective pressure at the macroscale reduces the local stress intensity factor at the microcrack tips (in a linear way, see Eq. (2)) and therefore dramatically reduce the crack growth rate. This reduction in crack growth rate is reflected in the macroscopic strain rate undergone by the sample.

To better compare the data obtained on different rock types and at different pressures, we will again employ the normalized stress

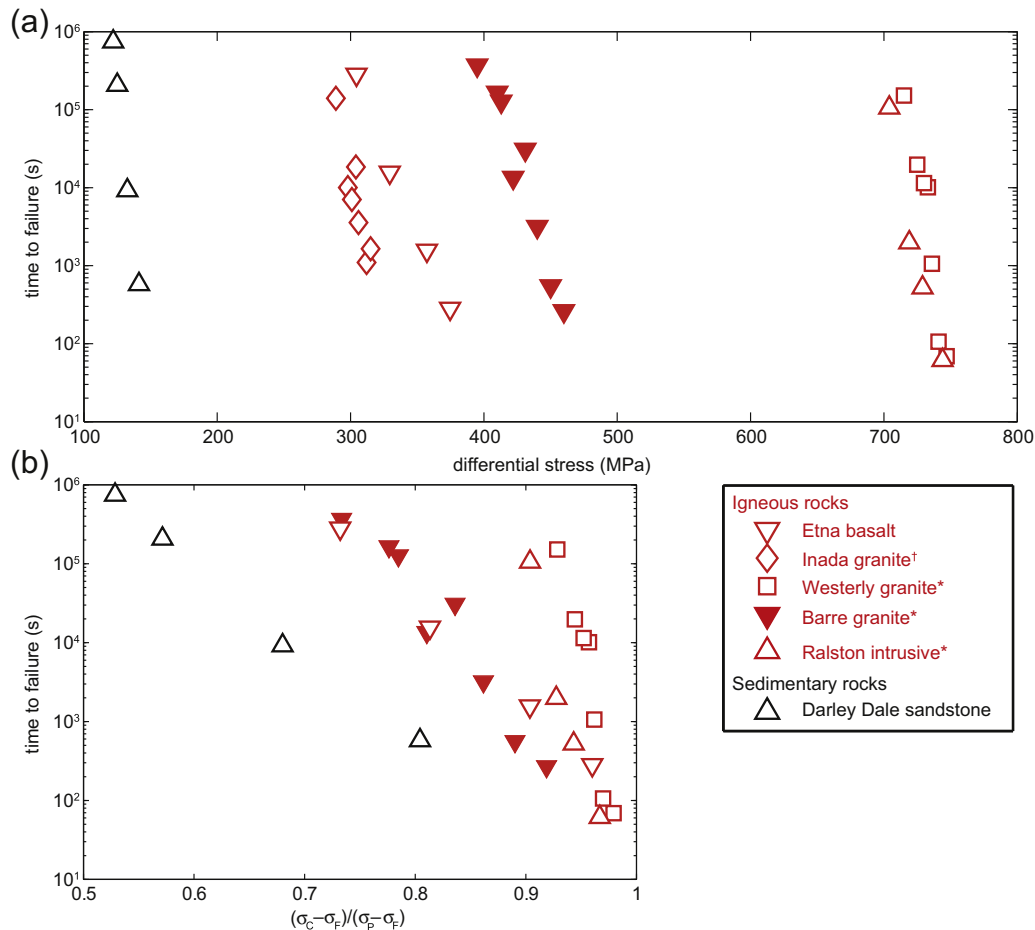


Fig. 7. Times-to-failure as a function of differential stress (a) and normalised stress (b) for various crustal rocks. Effective pressure was 30 MPa for experiments on Etna basalt (from Heap et al., 2011) and Darley Dale sandstone (from Heap et al., 2009a), (†) 10 MPa for experiments on Inada granite (from Fujii et al., 1999), (*) 50 MPa for experiments on Westerly granite and Ralston intrusive (Kurita et al., 1983).

defined in Eq. (7). In the previous section, the normalised stress took into account that the short-term peak stress and frictional strength are different for different rock types. Here, the normalisation also compensates for the change in short-term peak stress and frictional strength with increasing effective pressure, permitting meaningful comparisons. The normalised plots are shown in Figs. 9b and 10b. Again, when the frictional strength was not reported, we calculated it using a friction coefficient of 0.5.

Remarkably, the time-to-failure data of Kranz (1980) on Barre granite at ambient humidity conditions all follow a consistent trend in the normalized plot (Fig. 9b). This implies that the variations observed as a result of the change in effective pressure are well explained by the shifts in short-term and residual strength. Note, however, that the increase in total strain with increasing confining pressure (see strain data provided by Kranz, 1980) contributes to the observed time-to-failure: hence, the observed stress sensitivity of time-to-failure for various confining pressures may not necessarily mirror the stress sensitivity of the creep strain rate. For water-saturated rocks, the slopes of the creep strain rate curves decrease when the effective pressure is increased (Fig. 10b). In the normalized plot (Fig. 10b), this decrease in stress sensitivity with increasing effective pressure is apparent for Darley Dale sandstone. For Etna basalt, the creep strain rates at an effective pressure of 10 MPa are markedly higher and more stress sensitive than those at 30 and 50 MPa. This decrease in stress sensitivity of the creep strain rate with increasing effective pressure could result from an inhibition of stress corrosion reaction rate because of a reduction in

crack aperture, which would have two effects: (1) it would limit the diffusion of active species to the crack tips (Heap et al., 2009a), and (2) it would also reduce the overall crack density (i.e., the number of propagating cracks). In this regard, the similarity between strain rate sensitivities at $P_{\text{eff}} = 30$ MPa and 50 MPa in Etna basalt could be related to a critical pressure for crack closure slightly below 30 MPa; this is consistent with the pressure sensitivity of permeability in this rock, which is marked by a severe decrease above 30 MPa (Vinciguerra et al., 2005).

Our observations of the impact of effective pressure on creep, as discussed above, are restricted to the brittle field (i.e., all the aforementioned experiments end up by localised macroscopic failure by shear faulting of the samples). With increasing confining pressure, even at ambient temperature, rocks become ductile (Paterson and Wong, 2005): they can accommodate large strains through distributed deformation. For some rock types, such as sandstones, ductile deformation is driven by diffuse microcracking (cataclastic flow, see Wong et al., 1997). In this regime, subcritical crack growth is expected to play a role. However, there is, to our knowledge, no data describing such time-dependent effects in the cataclastic flow regime.

3.3. The influence of temperature

The influence of temperature on creep strain rate and time-to-failure is shown on semi-log plots in Figs. 11 and 12, respectively. For any given differential stress, an increase in temperature

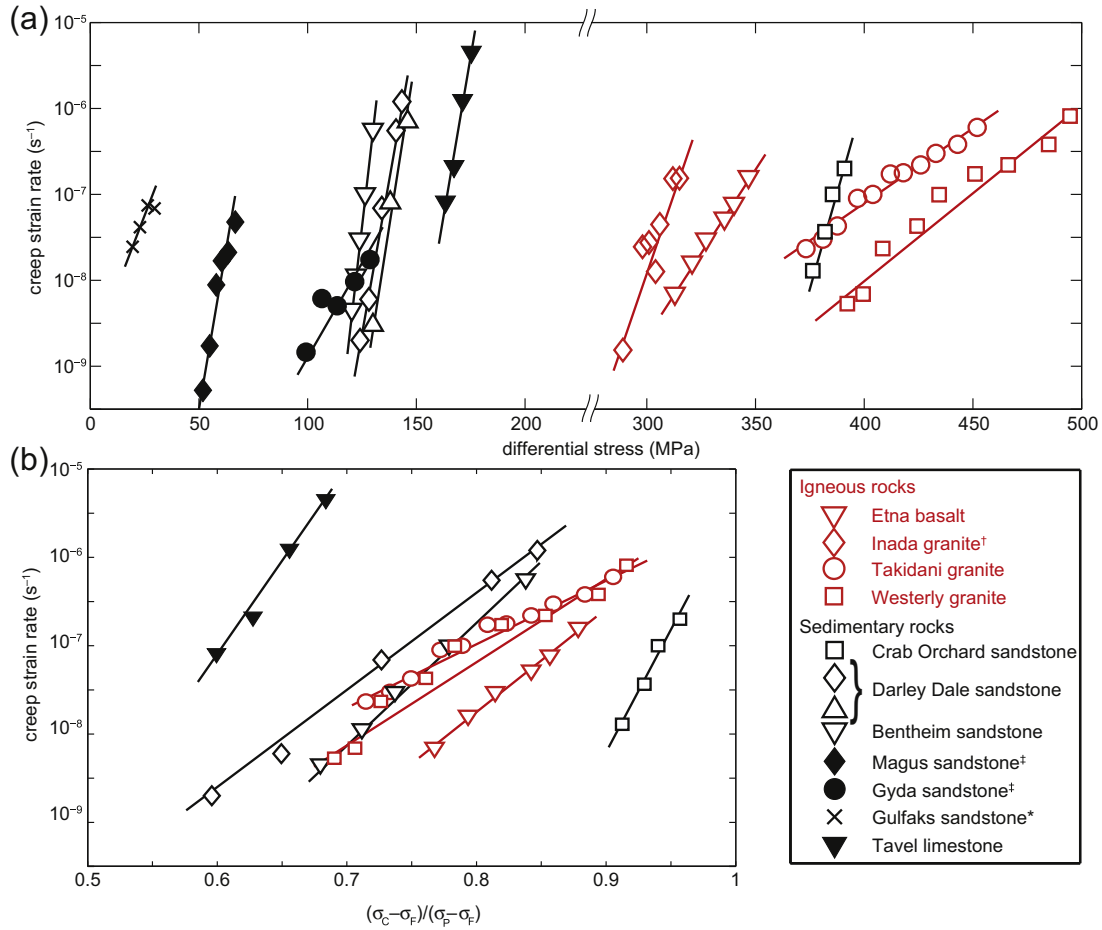


Fig. 8. Creep strain rates as a function of differential stress (a) and normalised stress (b) for a number of crustal rocks. All data are from stress-stepping creep experiments under the conditions of a 50 MPa confining pressure and a 20 MPa pore fluid (water) pressure (equating to an effective pressure of 30 MPa), except for (†) Inada granite (dry and under a confining pressure of 10 MPa), (‡) Magnus and Gyda sandstone (13.8 MPa pore fluid (brine) pressure and a 34.5 MPa confining pressure), and (*) Gulfaks sandstone (13.8 MPa pore fluid (brine) pressure and a 41.4 MPa confining pressure). Data is taken from: Etna basalt (Heap et al., 2011), Inada granite (Fujii et al., 1999), Takidani granite (this study), Westerly granite (Brantut et al., 2012), Crab Orchard and Bentheim sandstone (Heap et al., 2009b), Darley Dale sandstone (triangles: Baud and Meredith, 1997; diamonds: Heap et al., 2009a), Magnus, Gyda, and Gulfaks sandstone (Ngwenya et al., 2001), Tavel limestone (this study).

produces a substantial increase in creep strain rates in porous sandstones (Fig. 11a). For example, at a fixed differential stress of around 115 MPa, the creep strain rate in Bentheim sandstone increases by approximately three orders of magnitude as the temperature is increased from 25 °C to 75 °C. Similar increases are also

seen for the other sandstones in Fig. 11a. By contrast, previously unpublished data on Etna basalt show that, although still significant, the increase in creep strain rate is considerably smaller over the same temperature interval (Fig. 11b). The influence of temperature on time-to-failure follows a very similar trend: times-to-

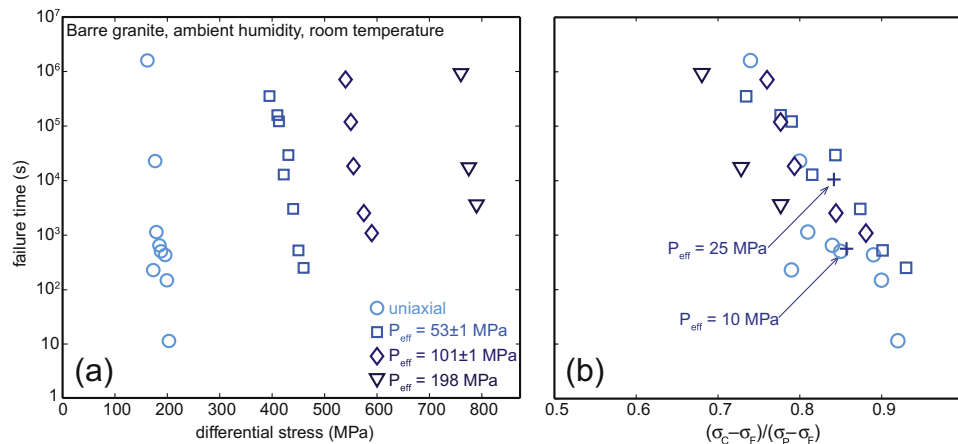


Fig. 9. Times-to-failure against differential stress (a) and normalised stress (b) for Barre granite under different effective pressures. Data taken from Kranz, 1980.

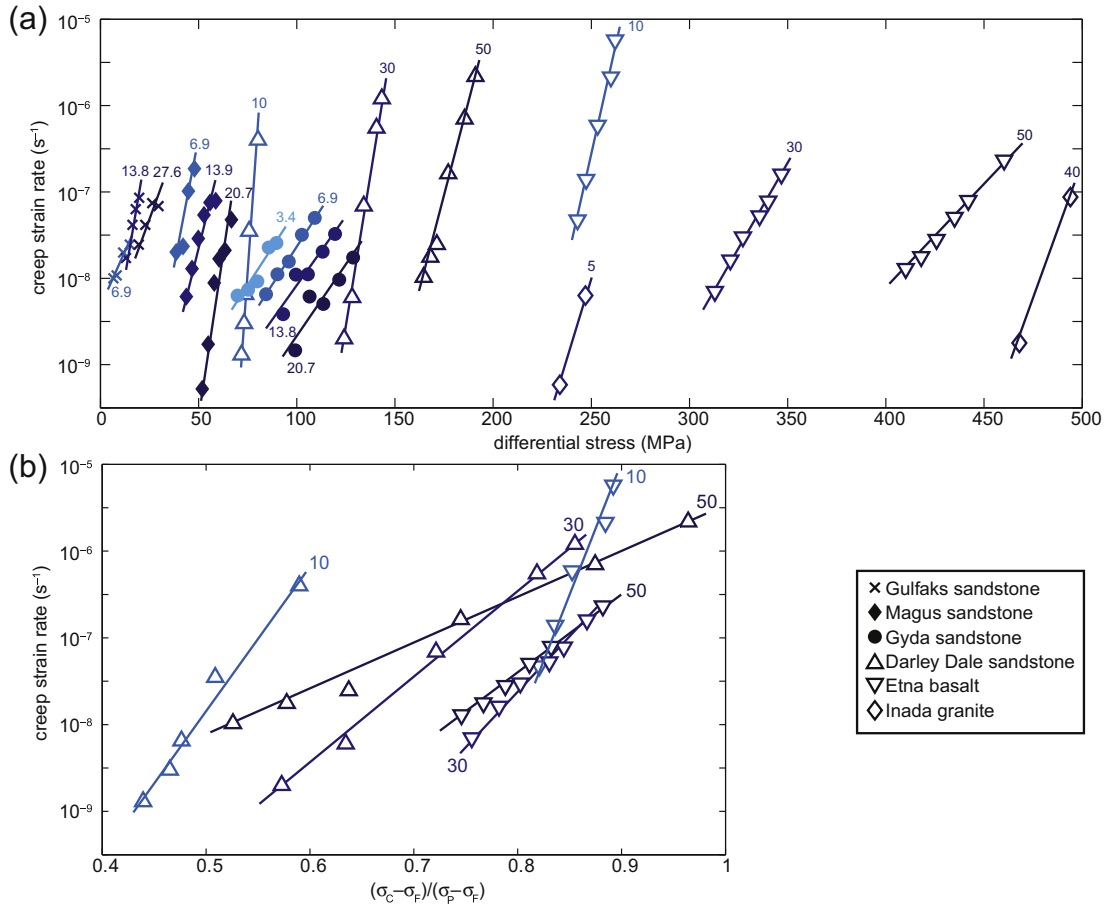


Fig. 10. Creep strain rates against differential stress (a) and normalised stress (b) for a number of crustal rocks under different effective pressures (labelled in MPa next to the curves). Data is taken from: Etna basalt (Heap et al., 2011), Inada granite (Fujii et al., 1999), Darley Dale sandstone (Heap et al., 2009a), Magnus, Gyda, and Gulfaks sandstone (Ngwenya et al., 2001).

failure decrease with increasing temperature. In Barre granite (Fig. 12; Kranz et al., 1982), the time-to-failure decreases by about two orders of magnitude as temperature is raised from ambient to 200 °C.

The observed influence of temperature on macroscopic strain rate and time-to-failure can be explained by the sensitivity of the rate of stress corrosion cracking to temperature. According to the theory of stress corrosion cracking (e.g., Freiman, 1984; Atkinson,

1984), temperature can affect crack growth rate in two ways. Firstly, it has been widely recognised that an increase in temperature induces an increase in crack growth rate in accordance with an Arrhenius relationship (e.g., Lawn, 1993, Chapter 5). Secondly, temperature can also affect the stress dependency of crack growth rate. These effects can be illustrated by using a subcritical crack growth law derived from chemical kinetics (e.g., Freiman, 1984):

$$v \propto \exp\left(\frac{-H + bK_I}{RT}\right), \tag{8}$$

where we recall that H is the activation energy, K_I is the stress intensity factor, b is a constant linked to crack tip curvature and the activation volume of the stress corrosion reaction, R is the gas constant and T is the absolute temperature. Inspection of Eq. (8) shows that an increase in temperature not only offsets the crack velocity, but also induces a decrease in the K_I dependency through the factor b/RT . Hence, the stress dependency of creep strain rate should decrease with increasing temperature. This trend is apparent for sandstones (Fig. 11a) as well as for Etna basalt (Fig. 11b), although we should treat this observation with some caution as the range of temperature investigated is very limited.

Precise experimental estimates of activation energy for the whole brittle creep process have been attempted (e.g., Kranz (1980) determined $H \approx 50$ kJ/mol for Barre granite). However, the effect of temperature on the stress sensitivity of subcritical crack growth rate greatly limits the validity of such estimates. Indeed, a global

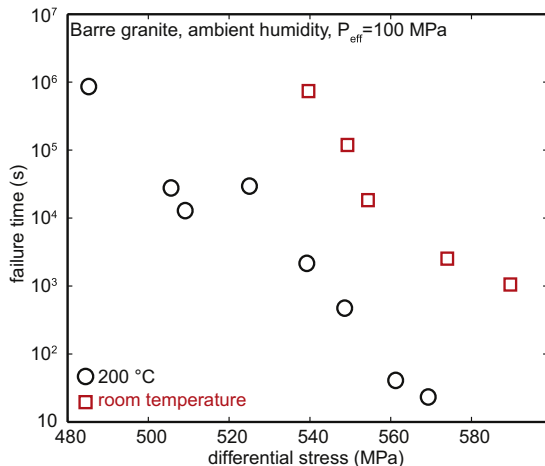


Fig. 11. Times-to-failure against differential stress for Barre granite at room temperature and 200 °C. Data taken from Kranz et al., 1982.

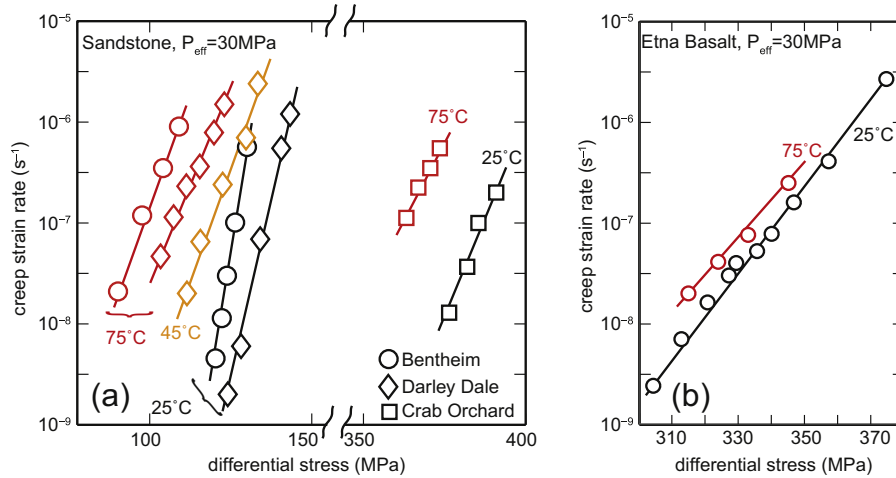


Fig. 12. (a) Creep strain rates against differential stress for three sandstones at different temperatures (indicated next to the curves; data taken from Heap et al., 2009b). (b) Creep strain rates against differential stress for Etna basalt at 25 and 75 °C.

activation energy linking directly the macroscopic strain rate to the temperature is ill-defined when the effect of temperature on the stress dependence is not deconvolved from the global behaviour. For instance, any activation energy calculated from the data of Fig. 11 would be stress-dependent and therefore not physically meaningful.

A full understanding of the effect of temperature on brittle creep would require both (1) a large dataset on a single rock type, exploring a wide range of temperatures, and (2) a precise description of the subcritical crack growth law (Eq. (4)).

3.4. Chemistry of the pore fluid

Stress corrosion is fundamentally a chemically activated process, associated with fluid adsorption on crack surfaces and fluid-assisted crack extension. The chemistry of the pore fluid potentially affects both of these processes. Firstly, surface adsorption affects the specific surface energy of the material. An important case is the effect of water as a pore fluid, which significantly decreases the specific fracture energy and hence the fracture toughness of sandstones (Baud et al., 2000). Although this is a short-term effect, it also affects the creep behaviour since a modification to the specific surface energy can also impact the stress range of stress corrosion cracking (see Rice, 1978).

Secondly, the stress corrosion reactions at crack tips are also affected by the chemical activity of the active species (e.g., water molecules). It is clear that stress corrosion can progress in rocks even at ambient humidity (for example, most of the triaxial data of Kranz is on granite samples at ambient humidity).

Experiments on Westerly granite (Kranz et al., 1982) have shown that times-to-failure are shorter by around three orders of magnitude under saturated conditions than under ambient humidity conditions (see Fig. 13). These observations can be explained by the lower chemical activity of water (measured by its partial pressure in a gas) in the latter condition, which slows down the stress corrosion cracking rate (e.g., Waza et al., 1980; Atkinson, 1984. See Fig. 1). It should also be noted that the transport kinetics of the active species at the crack tips will be different depending on whether there is a liquid phase or gaseous phase (ambient humidity), which could also impact crack growth rates.

More generally, the nature of the pore fluid (chemical composition, pH) is also expected to strongly affect the brittle creep strain rates. It has previously been demonstrated, for synthetic quartz, that subcritical crack growth rates increase as the hydroxyl (OH⁻)

concentration is increased, as the hydroxyl groups are attracted to the silicon sites (Si⁺) (Atkinson and Meredith, 1981). Similar effects have also been observed in glass (e.g., Wiederhorn and Johnson, 1972; Wiederhorn et al. 1982; Michalske and Freiman, 1983). There are currently no triaxial creep data documenting these effects in rocks. However, we can hypothesise that any variation in stress corrosion cracking rate due to a change in chemistry of the fluid will be reflected in a similar change in the macroscopic creep strain rate. An additional complexity in the case of macroscopic brittle creep is that the chemistry of the fluid may evolve as the fluid stays in contact with the rock. The crack network has a very large surface area in contact with the fluid, and the newly created crack surfaces are very reactive, which, over the long term, will bring the fluid increasingly closer to an equilibrium composition with the rock, independently from its initial composition. Clearly, further experimental investigations are needed to complement our current understanding of these processes.

3.5. Importance of microstructural state

As brittle creep is primarily driven by slow microcrack growth, it is expected that the crack density, porosity, and overall defect

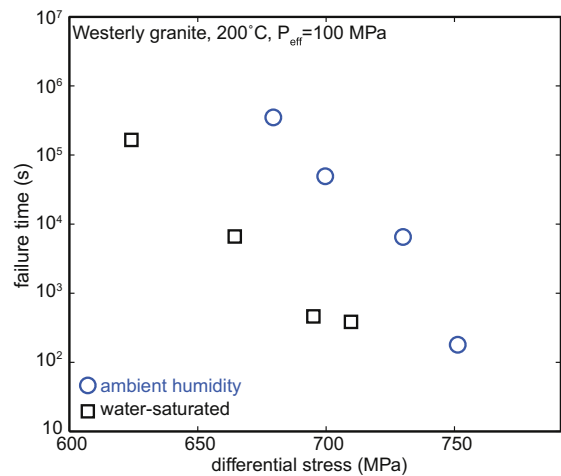


Fig. 13. Times-to-failure against differential stress for Westerly granite under saturated (blue circles) and ambient humidity (black squares) conditions. Data taken from Kranz et al., 1982.

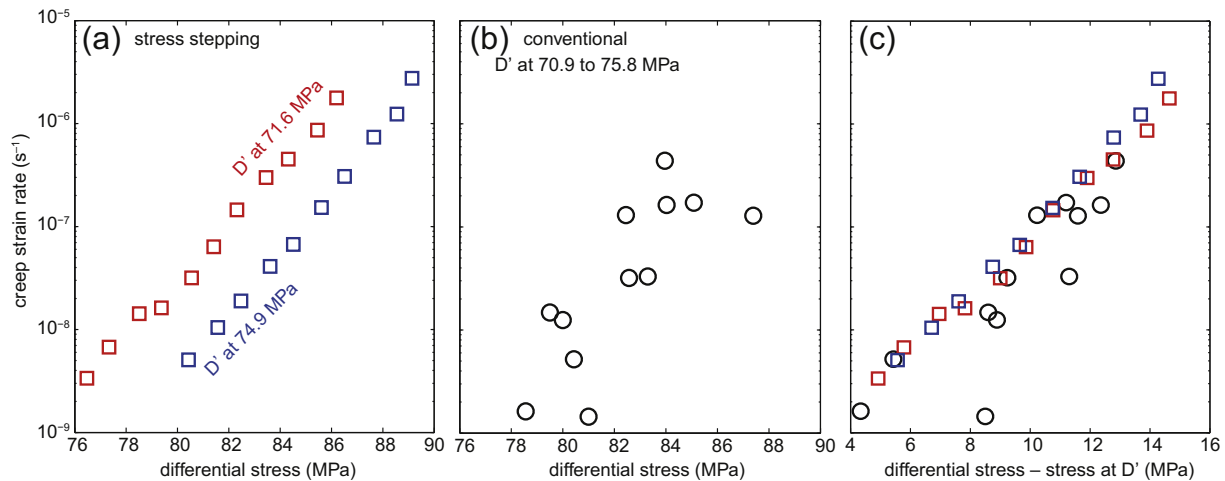


Fig. 14. Creep strain rate against differential stress for samples of Darley Dale sandstone deformed at 10 MPa effective pressure. (a) Stress-stepping tests. Stress at D' is reported on the graph. (b) Conventional tests performed on different samples. (c) Strain rate is plotted against the difference between differential stress and stress at D' .

structure of the rock, hereafter referred to as the “microstructural state”, will exert a strong influence on the creep strain rate. In particular, a material with a high level of initial defects (e.g., microcracks, pores, etc.) is expected to creep faster than the same material with a lower level of initial defects. As a corollary, any variability in the initial microstructural state (e.g., variation in porosity) is likely to be reflected in a large difference in creep strain rate (or time-to-failure) between different samples of the same rock deformed under the same conditions. More precisely, it is the microstructural state at the initiation of creep that will influence the creep strain rate. For a given rock type, this microstructural state is reflected in the position (in terms of strain and stress) of D' , which we recall is the point when deformation becomes dominated by dilatancy. In order to observe how the microstructural state influences brittle creep strain rates, we present here previously unpublished data from a suite of experiments on Darley Dale sandstone samples with different initial microstructural states (as indicated by differences in initial porosity), deformed at an effective pressure of 10 MPa. Creep strain rates as a function of stress are reported in Fig. 14. As expected, data obtained using the stress-stepping method show internal consistency (Fig. 14a), and we observe that when D' occurs at a higher stress then the strain rate is lower. By contrast, data from conventional tests (Fig. 14b) appear scattered because they are obtained from different samples with a range of initial microstructural states (the values of the stress at D' for each sample are listed in Table 2, and range from 70.9 to 75.8 MPa). Nevertheless, like the stress-stepping data in Fig. 14a, we observe that, for any given differential stress, samples for which D' occurs at higher stress generally creep slower than samples for which D' occurs at lower stress. These observations can be rationalised as follows. For two samples of the same rock type, a comparatively lower stress at D' in one sample implies that the stress required for dilatant cracking to become dominant is lower; we can thus infer that the overall number and/or size of defects (initial cracks, voids, grain boundaries etc.) is larger in that sample. This results in (1) a larger number of cracks subjected to subcritical crack growth, and/or (2) a faster growth rate of each individual crack. The combined effect leads to a higher overall strain rate.

Hence, if the creep strain rate is re-plotted as a function of the difference between the creep stress and the stress at D' then most of the data collapse onto a single line, as shown in Fig. 14c. This confirms that the stress at D' can be used as an empirical reference stress that accounts at least in part for the variation in the internal structure of the sample.

4. Dynamics of microfracturing during brittle creep

4.1. Coupling between subcritical and dynamic crack growth

In the brittle field, deformation is often associated with dynamic microfracturing events that can be recorded in the form of acoustic emissions (AEs; see for instance Lockner (1993a, b) for a comprehensive review of the subject). AEs are high frequency elastic wave packets generated by the rapid release of strain energy such as during brittle microfracturing. In this section we review the main observations of AEs during brittle creep under triaxial conditions, and discuss how they can be interpreted to improve our understanding of the dynamics of time-dependent fracturing in rocks.

During brittle creep, it is generally observed that the cumulative number of AEs and cumulative AE energy (defined as the integrated envelope of the AE signals) follow qualitatively the same trimodal trend as the strain (e.g., Lockner and Byerlee, 1977; Baud and Meredith, 1997). Specifically, the AE (and AE energy) rate decreases during primary creep, remains approximately constant during secondary creep, and increases during tertiary creep (Fig. 15). The approach to macroscopic failure at the end of tertiary

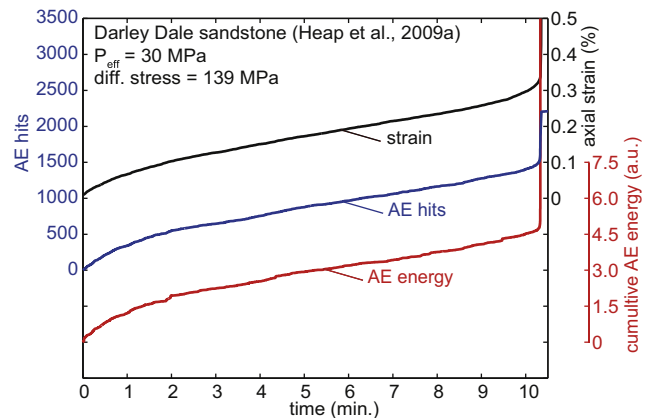


Fig. 15. Plots of axial strain (black), cumulative number of AE hits (blue) and cumulative waveform energy (red) as a function of time for a triaxial creep experiment conducted on Darley Dale sandstone, at an effective pressure of 30 MPa, and a differential stress of 139 MPa. After Heap et al., 2009a.

creep is generally associated with a dramatic increase in the AE rate. The occurrence of AEs, corresponding to *dynamic* microfracturing, in conjunction with *slow* subcritical cracking, appears counterintuitive but can be explained as follows. Firstly, subcritical crack growth itself can generate AEs if crack extension proceeds in a series of small, episodic steps, resulting in a slow average propagation rate (e.g., Sano, 1981). Secondly, even when a microcrack grows subcritically, it modifies the stress and strain in its surrounding region, and these modifications can generate local positive feedback that can trigger dynamic extension of neighbouring cracks. Hence, AE can be viewed as a normal consequence of subcritical crack growth. Because both slow and dynamic cracking induce deformation, it is then natural to observe that AE number follows the same trend as the macroscopic strain.

When the experimental arrangement allows an array of multiple AE transducers (typically 8–32) to be positioned around the sample, it is also possible to determine the spatio-temporal distribution of AE hypocentres during deformation (e.g., Lockner, 1993a,b). This allows the evolution of the deformation process to be followed in space and time. By analysing the spatial correlation of AE hypocentres during primary, secondary and tertiary creep, Hirata et al. (1987) determined that the spatial distribution of AEs was fractal, and that the fractal dimension decreased as the rock approached failure. They interpreted this decrease as indicating that AE sources were becoming more and more spatially clustered as macroscopic failure was approached. This is consistent with the observations of Lei et al. (2000, 2003), who showed that AE hypocentres were distributed throughout their rock samples in many small clusters during primary and secondary creep, but became progressively more localised along the nascent rupture plane during tertiary creep, as shown in Fig. 16.

Taken together, these observations suggest that tertiary creep originates from microcrack interactions, which generates strain localisation and results in shear faulting and macroscopic failure.

4.2. Microstructural state at the onset of tertiary creep

Brittle creep is controlled by the growth of cracks, and eventually results in macroscopic faulting of the rock. Despite differences in the control conditions between constant strain rate tests and brittle creep tests (performed at constant stress), the microscopic processes leading to macroscopic failure are the same. Macroscopic fracture is driven by the coalescence of many microcracks, followed by frictional sliding on the resulting fault (e.g., Paterson and Wong, 2005). In constant strain rate tests, this crack coalescence is marked by a macroscopic strain weakening behaviour, which starts at the peak stress. In brittle creep tests, where a peak stress does not exist,

it is marked by the tertiary creep phase, during which strain is accelerating towards failure. Experiments on quartzite and granite under uniaxial conditions (Kranz and Scholz, 1977) have shown that the onset of tertiary creep is marked by a critical dilatant volume change, the value of which depends on the fracture strength and the rock type. Experiments on Darley Dale sandstone (Baud and Meredith, 1997; Heap et al., 2009a) and Etna basalt (Heap et al., 2011) have confirmed this observation under triaxial conditions, and have shown that regardless of the imposed creep stress and the resultant strain rate in a particular creep experiment, the measured proxies for microstructural state (strain, AE energy and porosity change) at the onset of tertiary creep all fall in a remarkably narrow range of values for a given rock type and set of environmental conditions. This suggests the existence of a critical level of damage, or more generally, a critical microstructure, that can be sustained by a rock; with any further increase in damage above the critical state resulting in strain acceleration and failure. This critical microstructural state should, in theory, correspond to the onset of failure under both creep and constant strain rate conditions. In the latter case, the critical microstructural state should be related to the position of peak stress and/or to the onset of macroscopic strain localisation (which is, in general, a function of strain weakening rate, friction and dilatancy factors (Rudnicki and Rice, 1975)). It should be noted, however, that our definition of the critical microstructural state is primarily conceptual since it is related to the onset of macroscopic failure; the critical microstructure does not simply correspond to a scalar crack density and/or porosity, but must also involve information on the spatial clustering of cracks and crack lengths (Kachanov and Sevostianov, 2012).

4.3. Micro- and macro-structural observations

While indirect measurements, such as acoustic emission output and the evolution of ultrasonic wave velocities, can be used to detect microstructural changes during creep, the direct observation of microstructural evolution during creep presents a challenge. During a typical creep experiment, a significant and sometimes major proportion of the total strain (and acoustic emission energy) occurs during the initial loading of the sample to reach the level of creep stress. Therefore, analysing the microstructural changes that occur during the brittle creep phase would require us to distinguish between those cracks that formed during the initial loading, and those formed during creep. In practice, this is extremely difficult, if not impossible. Although cracks that have grown by stress corrosion sometimes present typical features, such as small, periodic steps produced by sequences of growth and rest (e.g., Sano, 1981),

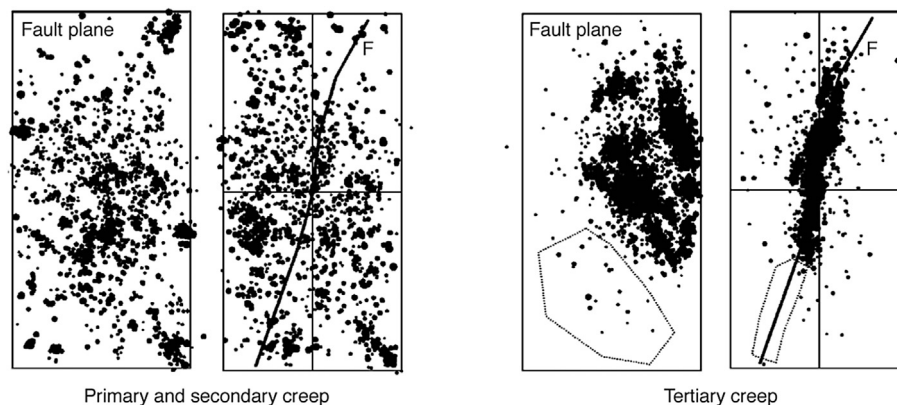


Fig. 16. Acoustic emission hypocentre locations during a stress-stepping brittle creep test performed on a jointed granitic porphyry sample. Left: events occurring during primary and secondary creep. Right: events occurring during tertiary creep. Modified from Lei et al. (2003).

such subtle features are likely to be overprinted by the dynamic damage (fast crack growth associated with local stress concentrations) occurring throughout creep. Furthermore, the dramatic acceleration of strain during tertiary creep, and the subsequent formation of a fault, will certainly mask any potential markers of slow crack growth during the preceding phases.

Despite these difficulties, some attempts have been made to investigate microstructural evolution during brittle creep. Heap et al. (2009a) performed microcrack density analysis on samples of Darley Dale sandstone following creep deformation. Their 2D analysis showed that, when compared with the undeformed material, crack density increased by between 24 and 37% and crack anisotropy increased threefold by the onset of tertiary creep. They concluded that creep is dominated by the growth of cracks sub-parallel to the maximum principal stress, entirely as expected for brittle deformation under triaxial conditions (e.g., Paterson and Wong, 2005). However, in Etna basalt, the same authors reported that the contribution of creep-related crack growth to the overall microstructure was so obscured by the pervasive network of pre-existing thermal microcracks that it rendered any quantitative microstructural analysis futile (Heap et al., 2011).

In general, the problem of overprinting is clearly unsolvable for post-failure observations. At the macroscopic scale (Fig. 17), it is evident that one cannot distinguish the sample fractured during a creep test (Fig. 17b) from the one fractured during a constant strain rate test (Fig. 17c). At the microscopic scale (Fig. 18), the fractures are also indistinguishable. The apparent difference in fault thickness and overall comminution between the fault produced during creep (Fig. 18b) and the one produced at constant strain rate (Fig. 18c) is an experimental artefact due to the larger fault displacement imposed in the latter case, which results from the loss of control of the loading device at the end of tertiary creep (Fig. 3).

5. Brittle creep models

A number of modelling approaches have been proposed to interpret and predict the mechanical behaviour of rocks during brittle creep. The essence of the problem in modelling brittle creep is to find a tractable way to link small scale microcrack growth with its macroscopic manifestation, i.e., creep strain and shear fracture. This upscaling problem has been a longstanding issue in rock mechanics (and in solid mechanics in general), and in particular the

process of crack interactions and coalescence to form a macroscopic fault remains enigmatic. A general discussion on these issues can be found in Paterson and Wong (2005), and we only review here the models that explicitly include time-dependent effects. Brittle creep models can be divided into three categories: phenomenological approaches, statistical approaches which include time-dependency in the form of local static fatigue, and micromechanical approaches which use fracture mechanics and subcritical crack growth applied to simplified crack geometries. It should be noted that these approaches can often be cooperative rather than competitive. We review the essential assumptions and results for each model category, and discuss representative examples.

5.1. Phenomenological approaches

Main (2000) has suggested that the apparent trimodal brittle creep behaviour (see for instance Fig. 6) of rocks could be explained by the interplay of two essentially independent processes operating simultaneously; one producing a positive feedback and the other producing a negative feedback on the creep strain. The starting point of Main's (2000) model is the following generalisation of the expression of the stress intensity factor at microcrack tips:

$$K_I \propto \sigma l^q, \quad (9)$$

where σ is the stress, l is the crack length and q is an exponent which is assumed to depend on the loading geometry and crack tip processes. A linear combination of two expressions like (9), one with a positive q to simulate a positive feedback between K_I and crack length, and one with a negative q to simulate a negative feedback, coupled with Charles' law ($dl/dt \propto K_I^p$), then produces a crack length versus time relation of the form:

$$l(t) = A(1 + t/T)^m + B(1 + t/t_f)^{-\nu}, \quad (10)$$

where A , B , T , m and ν are independent model parameters. In a final step, macroscopic observables such as strain or cumulative AE number are assumed to be proportional to crack size. A formulation like (10) produces trimodal creep curves, and the five parameters can be fitted to experimental data with a good agreement (e.g., Heap et al., 2009a). Such an approach is potentially useful as a tool

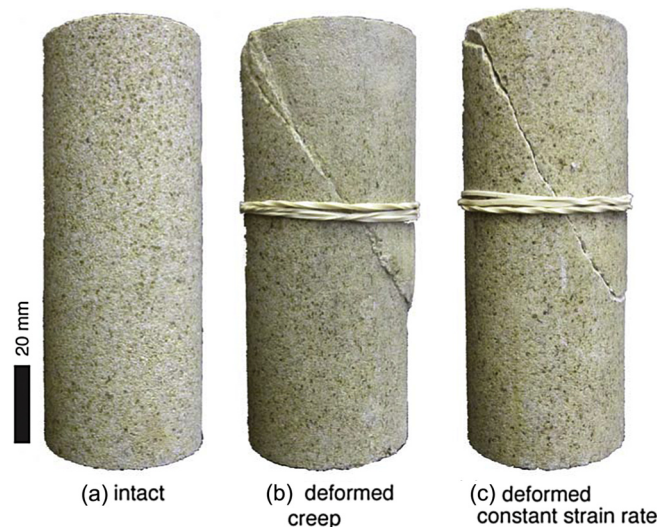


Fig. 17. Photographs of Darley Dale sandstone samples before deformation (a), after fracturing during a creep test (b) and after fracturing during a constant strain rate test (c). The initial diameter of the samples was 40 mm, and their initial height was 100 mm.

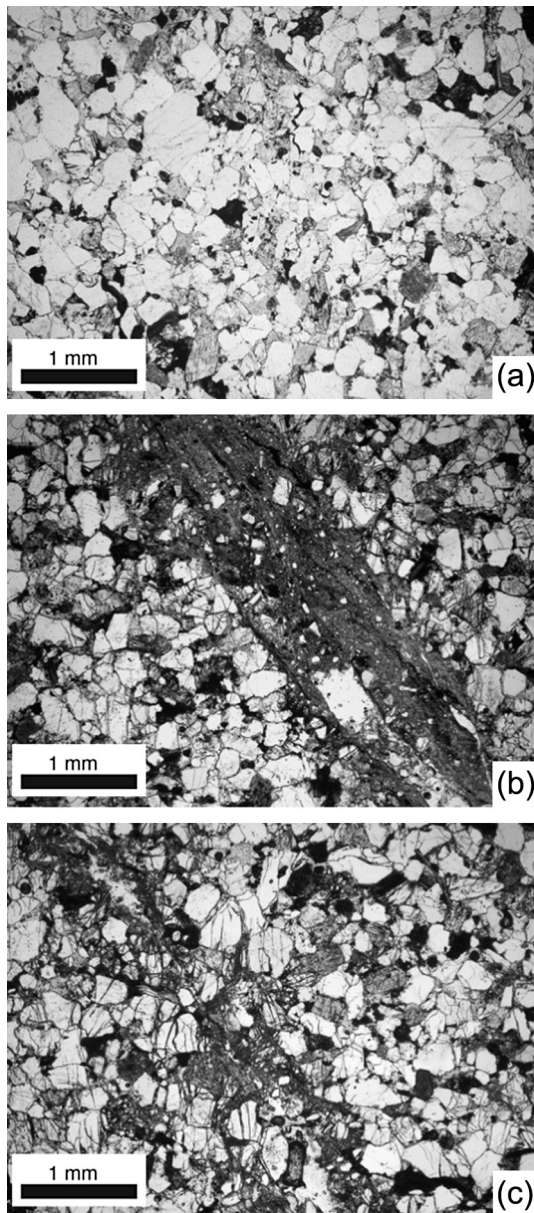


Fig. 18. Micrographs of Darley Dale sandstone samples under crossed-polars in transmitted light. (a) Intact sample, (b) sample fractured during creep and (c) sample fractured during a constant strain rate experiment.

to predict time-to-failure, as shown for instance by Bell et al. (2011). However, while the positive feedback process can be easily identified with the progressive microcrack growth (e.g., with $q = 1/2$ as in the case of remote uniaxial tension), the negative feedback process that produces strengthening remains physically unclear. In addition, the assumption that crack length is simply proportional to strain might be an oversimplification. As a result, the physical meaning of the five independent model parameters is not clear, and they are not easily related to independently measurable quantities (e.g., microcrack length or density).

5.2. Statistical models coupled to static fatigue

Creep models have also been constructed based on intrinsic heterogeneities in strength, time-to-failure and/or stress state within rocks. Such models are statistical (or probabilistic) in essence, and require the introduction of specific distributions of

heterogeneities (associated with a given spatial scale) within the material. The principle of these models is then to estimate how the successive failure or damage of individual rock elements, according to specified boundary conditions and local constitutive laws, can lead to the macroscopic creep and fracture observed in experiments. The early work of Scholz (1968b) constitutes one of the first successful attempts to model brittle creep of rocks using such a statistical approach. The starting point is to divide a macroscopic rock volume into small representative elements, which are subjected to local stresses according to a distribution $f(\sigma; \bar{\sigma})$ (where $\bar{\sigma}$ is the mean applied stress). Each element is assumed to follow a static fatigue law of the form:

$$\langle t \rangle = (1/\beta) \exp \left(H/RT + b(S^* - \sigma) \right), \quad (11)$$

where t is the time-to-failure of the element, H is the activation energy for the creep process, b is a constant corresponding to the stress sensitivity of the creep process, and S^* is the time-independent (short-term) strength of the element. Then, failure of an element is assumed to produce a macroscopic strain increment of amplitude η . Finally, it is assumed that elements in the rock fail independently from each other (i.e., non-interaction approximation). Under these assumptions, and provided that $f(\sigma; \bar{\sigma})$ is independent of σ , it can be shown that the macroscopic strain is:

$$\varepsilon = \eta(f(\sigma; \bar{\sigma})/b) \ln(t). \quad (12)$$

As shown by Scholz (1968b), this logarithmic relation between strain and time is overall compatible with experimental observations of primary creep. Further, the dependence of creep strain (and strain rate) on the applied stress $\bar{\sigma}$ is also consistent with data if a power law distribution $f(\sigma; \bar{\sigma}) \propto \bar{\sigma}^m$ is chosen. Because the model does not incorporate interactions between failed elements, there is no positive feedback and tertiary creep cannot therefore be predicted. For the same reason, there is no spatial organisation of the failed elements, i.e., no macroscopic strain localisation.

Such a model is significantly improved if interactions between elements can be taken into account. In other words, a physical description of how the stresses are redistributed after the failure of each element is needed. Such stress redistribution can be adequately described in one-dimensional cases by fibre-bundle models (e.g., Coleman, 1958), which were originally developed to understand tensile static fatigue in engineering materials. The principle of fibre-bundle models is that: (1) the stress applied to a material is distributed over a set of elements (one-dimensional fibres) which fail over time through a local static fatigue process (in the same fashion as Scholz's approach), and (2) the failure of a set of fibres redistributes the stress over the remaining fibres to maintain the applied stress (i.e., the supporting area decreases as elements fail). This physical description is rigorous for a one-dimensional medium undergoing tension, but needs to be adapted for materials in compression. Indeed, the strength of a failed element in compression is not zero but a complex function of the internal microcracks network. Turcotte et al. (2003) developed a one-dimensional model for rocks in compression based on a simple damage criterion. As in Scholz's (1968b) approach, the rock is divided into small representative volume elements, which are assumed to behave elastically, i.e., under uniaxial stress conditions:

$$\sigma = E\varepsilon, \quad (13)$$

where E denotes the Young's modulus of the element. Upon cracking, the element becomes "damaged", and its effective elastic moduli decrease. Following phenomenological damage mechanics models (e.g., Lemaitre and Chaboche, 1990), Turcotte et al. (2003)

assume that a damaged element sees its Young's modulus reduced by a constant fraction α (a so-called damage parameter). Hence the stress that a damaged element can support becomes:

$$\sigma = E(1 - \alpha)\varepsilon. \quad (14)$$

During creep, the damage parameter evolves from 0 (intact) to 1 (broken) through time according to some specific evolution law parameterised by the applied stresses, strain and/or temperature, while the remotely applied stress is redistributed across all the elements in the same fashion as in the fibre-bundle model. This produces a positive feedback and hence a progressive acceleration that corresponds to tertiary creep.

The one-dimensional model of Turcotte et al. (2003) was further developed to 2D by Amitrano and Helmstetter (2006) (or, more recently, by Xu et al., 2012), who computed the full 2D (plane strain) stress distribution using finite elements. In their approach, discrete increments in the damage parameter occur in a rock element according to both a time-independent Coulomb failure criterion, and a time-dependent static fatigue criterion (either an exponential form similar to Eq. (11) or a power law form). In their approach, damage is progressive, and a single element can undergo several “damage events”, which are assumed to successively reduce the time-to-failure. Fig. 19a shows an example of strain–time curve resulting from their model, obtained at a constant applied stress equal to 80% of the short-term strength (retrieved from a simulation using only the local Coulomb failure criterion). The model successfully reproduces the typical shape of creep curves, and it appears that the choice of exponential or power law static fatigue criterion does not qualitatively influence the results. Fig. 19b shows the spatial distribution of the damage parameter at the end of the simulation, using a power law static fatigue criterion. Damage (and hence strain) is localised within an oblique zone resembling the macroscopic fracture observed in experiments. In the model (using an exponential stress dependence for time-to-failure as in Eq. (11)), the primary creep strain can be approximated by:

$$\varepsilon = \frac{\bar{\sigma}}{E} \exp\left(-\frac{a}{\ln(\beta t)}\right), \quad (15)$$

where β is the characteristic rate introduced in Eq. (11), $\bar{\sigma}$ is the applied stress, and a is a parameter linearly dependent upon the stress sensitivity b and the applied stress $\bar{\sigma}$. The positive feedback between damage and time-to-failure of the elements introduced in the model also allows estimation of the tertiary creep phase in the non-interactive case. The tertiary creep strain can thus be estimated by an expression of the form:

$$\varepsilon = \frac{\bar{\sigma}}{E} \frac{1 - \alpha_0}{1 - t/t_c}, \quad (16)$$

where α_0 is the reference damage increment, and t_c is the macroscopic time-to-failure. According to Eq. (16), the strain rate in tertiary creep has a power law singularity with an exponent 2 as the material approaches failure. The full numerical simulations, which include stress redistribution, indicate that the power law exponent is in fact close to 1.3. These estimates are of great practical importance since they can easily be compared with experimental data, and potentially applied to predict time-to-failure at the field scale.

Statistical models such as those described above can successfully reproduce the creep phenomenology, and their parameterisation is physically sound. However, several major drawbacks arise from (1) the assumption of a static fatigue law, instead of a more physically grounded stress corrosion law, and (2) the damage mechanics approach, which is essentially phenomenological. In fact, the damage parameter α cannot be rigorously related to a well-defined microcrack density, and the effect of microcracks on elastic moduli are in general much more complex than the simple linear law assumed in Eq. (14) (Kachanov, 1993). In addition, it has been shown (Kachanov and Sevostianov, 2012) that the effect of microcracks on the effective elastic moduli is generally unrelated to their effect on the strength.

5.3. Micromechanical models

Other approaches, based on fracture mechanics, have also been suggested to explain and potentially predict how brittle creep operates. In general, these micromechanical approaches attempt to determine (with various approximations) the stress intensity factor at microcrack tips, depending on the applied stresses and a particular crack configuration. Then, the microcrack growth rate is calculated using a stress corrosion law. Finally, the connection between the microcrack length and the macroscopic strains is established using either thermodynamical approaches (Rice, 1975) or summation of individual strains (in the non-interaction approximation). Kachanov (1982a, b, c) determined exact solutions for the strain rate associated with the subcritical growth of mode I (tensile) cracks from the edges of initially sliding mode II flaws (sliding wing cracks, see geometry in Fig. 20) in elastic materials. Neglecting elastic interactions between cracks, the mode I stress intensity factor at the tips of the wing cracks is expressed in 2D as (Kachanov, 1982b):

$$K_I = 1.15 F_n \sqrt{\pi a} - \sigma' \sqrt{\pi l/2}, \quad (17)$$

where F_n is the stress driving the sliding on the initial flaw (which is an increasing function of the remotely applied differential stress), a

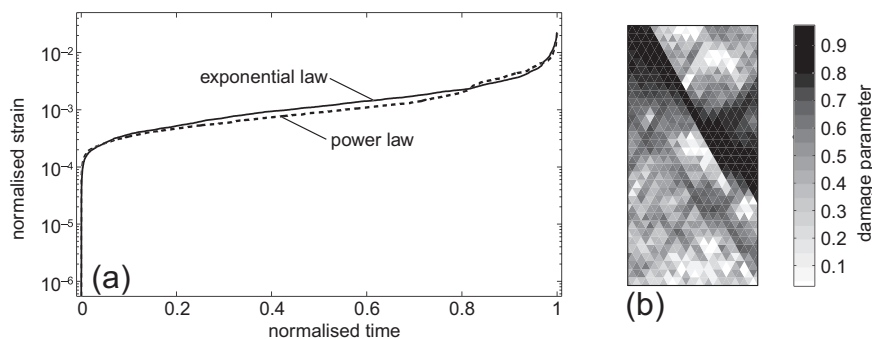


Fig. 19. Example of strain–time curve (a) and final distribution of damage (b) resulting from the 2D model of Amitrano and Helmstetter (2006). The applied creep stress is 80% of the short-term strength. An exponential law (solid line) or power law (dotted line) can be used for the stress dependence of time-to-failure. The damage distribution (b) corresponds to the power law case, but does not significantly depend upon the particular choice of the static fatigue law. Redrawn from Amitrano and Helmstetter (2006).

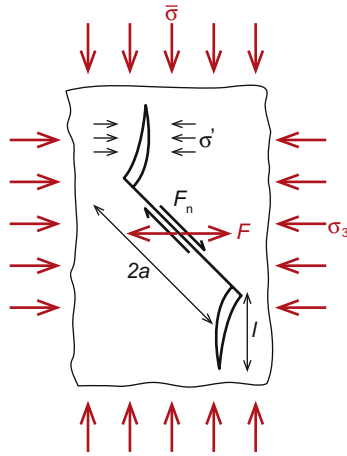


Fig. 20. Schematic of the wing crack model. The initial sliding flaw has a length $2a$, and mode I “wings” of length l open at its tips. F_n denotes the sliding frictional stress and σ' denotes the stress acting perpendicular to the wings (as defined by Kachanov, 1982a,b,c). Also reported are the remotely applied axial and lateral stress $\bar{\sigma}$ and σ_3 , respectively, as well as the resulting “wedging” force F acting at the center of the initial flaw, as defined by Ashby and Sammis (1990).

is the initial sliding flaw size, and σ' is the normal stress acting on the mode I cracks (proportional to the confining pressure). Expression (17) shows that the growth of mode I cracks under all-round compressive stress conditions is stable, i.e., increasing crack length (l) induces decreasing stress intensity factor at crack tips. Hence, when coupled to a stress corrosion law (such as Charles’ law, see Fig. 1), it is found that the crack growth rate decreases with increasing time. This process explains qualitatively well the primary creep phase, during which strain rate gradually decreases with accumulating strain (see Fig. 21a, solid line). Using a similar approach with an array of sliding wing cracks, Kemeny (1991) calculated the strain rate associated with subcritical crack growth (using Charles’ law), still neglecting interactions between cracks, and found that the axial strain during primary creep was proportional to the logarithm of time:

$$\epsilon = \epsilon_0 + C_1 \ln(1 + C_2 t), \quad (18)$$

where ϵ_0 is the elastic strain, C_1 is a constant proportional to the applied stresses, and C_2 is a power law function of the applied stress, with an exponent equal to the stress corrosion index. Eq. (18) is qualitatively similar to the formulation given in Eq. (12) determined by Scholz (1968b) from a radically different approach. A significant advantage of the formulation obtained from the micromechanical approach of Kemeny (1991) is that all the parameters are related to physically measurable quantities. In a similar fashion, Lockner (1993a, b) determined approximate solutions for the volumetric strain rate associated with subcritical crack growth in Westerly granite, also neglecting interactions between cracks. Since they both neglect crack interactions, the formulations of Kemeny (1991) and Lockner (1993a, b) are not able to reproduce the acceleration of strain in the tertiary creep phase.

As pointed out previously, the key problem in micromechanical models is determining a tractable way to account for elastic interactions between cracks. Because these interactions strongly depend on the spatial distribution of cracks, their orientations, size, and particular geometry, there cannot be a general rigorous way to achieve the description of interactions. All the models incorporating crack interactions use various simplifying assumptions. Costin (1985) developed a micromechanical model based on a collinear array of cracks, for which reasonable approximations of

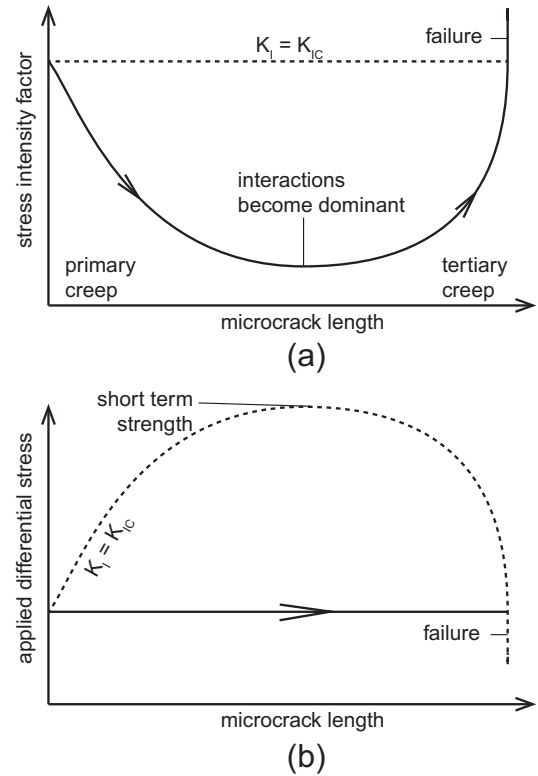


Fig. 21. Schematic of the evolution of stress intensity factor at microcracks tips (a) and applied differential stress (b) as a function of microcrack lengths, for creep conditions (solid lines) and constant strain rate conditions (dotted lines). Arrows indicate time evolution during creep.

elastic interactions can be made, and determined that, when interactions become dominant, the stress intensity factor becomes an increasing function of crack length, hence producing the runaway instability that leads to macroscopic failure (i.e., coalescence of the cracks; see Fig. 21a, solid line). Lockner and Madden (1991a, b) developed a two-dimensional model in which elastic interactions are approximated numerically and solved by applying a “Renormalisation Group” theory approach. Their model requires the description of an initial distribution of microcracks, which are positioned and allowed to grow only along a predefined regular network. This model is able to reproduce the primary and tertiary creep phases, as well as strain localisation in the form of microcrack clustering. However, due to the numerical procedure involved, simple analytical estimates of creep strain rates in connection with the parameters of the subcritical crack growth law are not available. Another approach was used by Yoshida and Horii (1992) in a model based on sliding wing cracks, in which they assumed that macroscopic failure would occur at a given critical microcrack length. By fitting this unique parameter to Kranz’s (1979, 1980) data on Barre granite, they were able adequately to reproduce the observed times-to-failure under various pressure and temperature conditions. However, such an approach is not able to reproduce the accelerating creep phase: in this framework failure occurs suddenly, which is not consistent with observations. A similar approach was followed by Lockner (1998), who extended his earlier work (Lockner, 1993a,b) to incorporate macroscopic fracture at a threshold axial inelastic strain. Using all the available data on Westerly granite, Lockner (1998) developed a semi-empirical constitutive law for this rock, including temperature and time effects in both the homogeneous (pre-failure) and the fractured material. The connection between homogeneous deformation and frictional sliding (described with a rate-and-state law) was

established empirically, following observations of strain weakening during fault formation. Because of this connection, the full model adequately reproduces the three stages of brittle creep. However, a serious drawback of this model is the need to constrain empirically at least seven independent parameters, including the critical inelastic strain at the onset of failure.

A very successful approach to microcrack interactions is the one developed by Ashby and Sammis (1990), and further extended by Deshpande and Evans (2008) and Bhat et al. (2011). In their model, Ashby and Sammis accounted for crack interactions in a global way, by adjusting the effect of confining pressure as axial cracks grow, thus reflecting the decrease in supporting area perpendicular to the cracks (in that sense, the model is inspired by the fibre-bundle models). They express the mode I stress intensity factor at the crack tips, in 2D (see Fig. 20), as

$$K_I = \frac{F}{\sqrt{\pi(l + \beta a)}} - (\sigma_3 - \sigma_3^i(l))\sqrt{\pi l}, \quad (19)$$

where F is the equivalent “wedging” force acting on the initial flaw (which depends on the friction coefficient on the flaw and the applied stresses), β is a numerical correction factor to ensure that K_I reduces to the exact expression for $l = 0$, σ_3 is the minimum principal stress (i.e., the confining pressure), and σ_3^i is the term corresponding to stress interactions, and is an increasing function of crack length (l). The original model of Ashby and Sammis (1990) was developed using $K_I = K_{IC}$ as a crack growth criterion, and provided a reasonable fit to the observed short-term strength of brittle rocks. Brantut et al. (2012) extended this time-independent micromechanical model by accounting for subcritical crack growth (i.e., replacing the $K_I = K_{IC}$ criterion by a relation like Eq. (1)), in order to determine how brittle creep stress and strain rate are related to the short-term mechanical behaviour of the rock. The relation between the applied stress (imposed as constant during creep tests, or varying during constant strain rate tests), the stress intensity factor (variable during creep tests, constant (equal to fracture toughness) during fast, constant strain rate tests) and crack length is depicted schematically in Fig. 21. When crack propagation is driven by the time-independent Griffith criterion ($K_I = K_{IC}$, dotted line), stress has first to be increased to induce further crack propagation, until it reaches a peak (short-term strength), and then becomes a decreasing function of crack length. The peak stress corresponds to the short-term (time-independent) strength, and is achieved when the interaction term becomes dominant. By contrast, during creep, when a constant stress is imposed (solid line), the stress intensity factor at crack tips initially decreases with increasing crack length (i.e., with increasing strain): crack interactions are not dominant and the behaviour is qualitatively similar to the case of isolated cracks. When coupled to a stress corrosion law, this implies that the crack growth rate decreases, thus producing a decreasing strain rate (primary creep). However, at some threshold in crack length, crack interactions become dominant (the term $\sigma_3^i(l)\sqrt{\pi l}$ is larger than $\sigma_3\sqrt{\pi l}$ in Eq. (19)), and the stress intensity factor increases with further crack propagation. The stress corrosion law then implies that the crack growth rate increases, thus producing an increasing strain rate (tertiary creep). In such a framework, the crack length (or, equivalently, strain) at which interactions become dominant is approximately the same in the time-independent case ($K_I = K_{IC}$, variable stress) and in the time-dependent creep case (variable K_I , constant stress). The minimum in K_I corresponds to the minimum in crack growth rate, and hence is approximately close to the minimum in macroscopic strain rate (i.e., it is the secondary creep strain rate as defined previously). Using the correspondence between the crack length at peak stress and at the minimum K_I , Brantut et al. (2012) were able to determine a simplified relationship between the creep strain rate $\dot{\epsilon}$, the applied stress $\bar{\sigma}$,

the short-term strength σ_p and the parameters of Charles' law, such that:

$$\dot{\epsilon} \propto e^{-\frac{H}{kT}} \left(1 - k \frac{\bar{\sigma} - \sigma_p}{K_{IC}/\sqrt{\pi a}} \right)^{n+1}, \quad (20)$$

where we recall that H is the activation enthalpy of the stress corrosion reaction, R is the gas constant, T is the absolute temperature, $\bar{\sigma}$ is the remotely applied axial stress, σ_p is the short-term strength, K_{IC} is the fracture toughness of the material, a is a characteristic initial crack size (commensurate to the starting grain size of the rock), k is a nondimensional parameter, of the order of 0.13 for Westerly granite, and n is the stress corrosion index of Charles' law. This approximate creep law produces very reasonable fits to data obtained in brittle creep experiments on Crab Orchard sandstone and Westerly granite, with stress corrosion indices comparable to those independently measured in single crack tests by Atkinson (1984).

Micromechanical models have the advantage of producing predictions based on physically measurable (or inferable) parameters, but those predictions are limited by the complexity of microcrack interactions (exact interactions can rarely be calculated), and they do not account for the real complexity of rocks (multi-mineralic assemblages, distribution of initial flaws, etc.). In addition, no micromechanical model is yet able to reproduce strain localization in a general way. Hence, all such models can only be viewed as useful guides to understanding experimental data, and predicting order of magnitude estimates for strain rates as a function of physical conditions.

5.4. Perspectives in brittle creep modelling

We have seen that, although much effort has been put into attempts to model brittle creep, there is currently no model that includes all the physical processes and observations in a realistic way. Existing phenomenological and statistical model are limited by the use of *ad hoc* assumptions on local time-dependent constitutive properties, and numerous independent, loosely constrained parameters can be tuned to produce a wide range of behaviour. Micromechanical models have the potential to be better constrained, since their parameters often have a clear physical meaning, but their mathematical complexity precludes a rigorous treatment of crack interactions and hence of macroscopic strain localization. In order to progress further, new and innovative approaches are needed to investigate the links between local subcritical crack growth, macroscopic strain rate, damage accumulation and strain localization. Another key independent factor is the knowledge of a precise description of the stress corrosion law (Eq. (4)): because models typically aim at making predictions for timescales much longer than those in experiments, the choice of the stress corrosion law is crucial. In particular, the modelled long-term strain rates and times-to-failure can be biased by several orders of magnitude if an inappropriate description is chosen.

6. Implications of brittle creep for the dynamics of the Earth's crust

Stress corrosion-driven crack growth has been reported in a very wide range of rocks (e.g., Atkinson, 1984). Less work has been done on brittle creep under triaxial conditions, however all rocks that have been tested to date have exhibited time-dependent creep in the presence of water as a pore fluid. It can therefore be considered to be a universal deformation mechanism and likely to

be ubiquitous in the brittle crust, and have important implications for crustal evolution and dynamics.

6.1. Strength of the upper crust

As stated in the [Introduction](#), fracturing controls the deformation of rocks under upper crustal conditions. Brittle creep allows rocks to deform and fail at stresses much lower than the critical, time-independent strength they would normally have in the absence of stress corrosion. Hence, it is reasonable to infer that brittle creep affects the overall strength of the crust. Asymptotically, for very long timescales, the strength of an intact rock should be the minimum stress at which brittle creep is able to proceed and lead eventually to macroscopic fracture. Following our earlier discussion (Section 3.1), a lower bound for this stress is the frictional strength. In other words, brittle creep (driven by stress corrosion) reduces the cohesion of intact rocks, but does not directly affect their internal friction. This implies that the maximum *long-term* strength of the crust must be controlled primarily by friction, *even in nominally intact rock*. Indeed, all *in-situ* stress measurements in boreholes indicate that stress in the crust is bounded by the frictional strength (e.g., [Zoback and Zoback, 1980](#); [Zoback and Healy, 1992](#); [Brudy et al., 1997](#); [Zoback et al., 2003](#)). Thus, brittle creep can be viewed as one of the fundamental mechanisms that allow crustal stress to be maintained at or below the frictional strength.

6.2. Dynamics of faulting during the earthquake cycle

If local stresses vary over short timescales, as is expected immediately before and after earthquakes, brittle creep is also likely to play a role in the short-term, by accommodating the induced stresses and strain in a time-dependent fashion.

[Perfettini and Avouac \(2004\)](#) used a brittle creep model in the form of a rate-and-state law (similar to that of [Lockner, 1998](#)) to model the post-seismic relaxation and aftershock rates that occurred after the 1999 Chi-Chi earthquake. From this, they were able to reproduce the first order features observed in the geodetic and seismological data.

A further situation where creep deformation is likely to be of particular importance is in association with the static stress changes that occur in a lobate pattern adjacent to faults following earthquake rupture. Such stress changes are very small and are generally of the order of only a few tenths of an MPa (a few bars) at distances of a few kilometres ([King et al., 1994](#)). Nevertheless, the extreme dependence of creep strain rate on differential stress means that even these small changes in differential stress could result in an increase or decrease in the local creep strain rate by as much as a factor of five or ten. Clearly this therefore has the potential to be a significant factor in the approach to failure of any fault strand within the stressed lobe.

6.3. Relations with other creep mechanisms under upper crustal conditions

Having commented on where we consider creep deformation to be important in the crust, it is also important to consider the effective lower limit where creep may cease to be important; that is, where other deformation mechanisms become faster and more dominant. Single crack stress corrosion experiments have shown that stress corrosion cracking can occur at levels of K_I down to below 50% of K_{IC} . As explained above, for stress corrosion-driven brittle creep we hypothesize that the effective lower limit occurs when the applied creep stress is equal to the frictional strength of the rock (for example, this occurs at a differential stress of 85 MPa

or 55% of the short-term peak stress for the experiment on Darley Dale sandstone shown in [Fig. 2](#)). Extrapolating the Darley Dale sandstone data of [Fig. 10](#) to this value of differential stress yields a creep strain rate close to 10^{-14} s^{-1} ; a rate commonly considered typical for long-term tectonic strain. We therefore need to ask whether stress corrosion-driven creep strain rates of this magnitude are ever likely to occur in the crust, or whether other deformation mechanisms are more likely to dominate the overall deformation under these conditions. [Brantut et al. \(2012\)](#) have performed theoretical calculations on this problem, and provided deformation mechanism maps for Crab Orchard sandstone which show that the transition from stress corrosion creep to pressure solution creep occurs at a strain rate of 10^{-13} s^{-1} for dissolution-limited pressure solution ([Niemeijer et al., 2002](#)) and 10^{-9} s^{-1} for diffusion-limited pressure solution ([Rutter, 1983](#)). The transition from stress corrosion-driven creep to pressure solution-driven creep has been observed experimentally in Crab Orchard sandstone deformed at 400 °C by [Rutter and Mainprice \(1978\)](#), who determined a strain rate of the order of 10^{-9} s^{-1} at the transition. However, there is currently no corpus of experimental data systematically documenting this transition over any realistic range of pressure and temperature conditions.

Throughout this paper, we have repeatedly alluded to frictional strength as the effective lower stress limit for brittle creep. However, it is well known that frictional properties of rocks are also time-dependent ([Scholz, 2002](#)). The connection between brittle creep in intact rocks and frictional sliding in fractured rocks is not yet fully understood ([Lockner, 1998](#)). However, because frictional sliding at small scale requires fracturing of grains and asperities, it is likely that stress corrosion cracking plays a role in the macroscopically observed time-dependent frictional strength. In such a framework, time-dependent friction and brittle creep would be linked and present a range of common features. Indeed, [Lockner \(1998\)](#) pointed out that both phenomena follow the same macroscopic logarithmic relation between stress and strain rate. However, further work is needed to establish whether such connections are fortuitous or the result of a common microscopic mechanism.

6.4. Perspectives

Our understanding of the range of crustal depths over which stress corrosion creep is an important deformation mechanism remains only partial. This arises for two main reasons. Firstly, as we have already noted, current creep models are unable to capture all of the details and complexity of the creep process, and cannot therefore be used with confidence to extrapolate laboratory-derived data to tectonic strain rates. Secondly, the practicable timescales for conducting laboratory creep experiments means that the range of accessible strain rates is necessarily rather limited. The non-linear nature of the relation between applied stress and creep strain rate means that low stress, hence low strain rate, experiments would need to be conducted over durations of multiple months or years. This is simply not feasible in a normal laboratory setting where it would be scientifically and economically inefficient to tie up an expensive triaxial testing system for several years to produce one extra data point.

Therefore, to answer the key question, we need to develop better models that more accurately and rigorously describe the complexities of the brittle creep process, and then run experiments at lower strain rates in order to test the model predictions. This last point is currently being addressed through novel experiments that use the stable environment of the deep sea to allow ultra-long-term (months to years) brittle creep experiments to be run at strain rates that bridge the gap between laboratory and tectonic rates ([Meredith et al., 2011](#)).

Acknowledgements

We gratefully acknowledge Neil Hughes, Steve Boon, and John Bowles for their assistance and support during experimentation. We have benefited from discussions with Andy Bell, Ian Main, Sergio Vinciguerra, and Olivier Lengliné. We thank Chris Scholz and Yves Guéguen for their careful and insightful reviews of the manuscript. N. Brantut and P. Meredith were partly funded by UK NERC grant NE/G016909/1 "Time-dependent deformation: bridging the strain rate gap in brittle rocks". P. Baud and P. Meredith acknowledge the support of CNRS PICS grant. Patrick Baud was also partially funded by ANDRA under the FORPRO framework. Our thin sections were skillfully prepared by David Mann (High Mesa Petrographics).

References

- Amitrano, D., Helmstetter, A., 2006. Brittle creep, damage, and time to failure in rocks. *J. Geophys. Res.* 111. <http://dx.doi.org/10.1029/2005JB004252>.
- Anderson, O.L., Grew, P.C., 1977. Stress corrosion theory of crack propagation with applications to geophysics. *Rev. Geophys. Space Phys.* 15, 77–104.
- Ashby, M.F., Hallam (née Cooksley), D., 1986. The failure of brittle solids containing small cracks under compressive stress states. *Acta Metall.* 34 (3), 497–510.
- Ashby, M.F., Sammis, C.G., 1990. The damage mechanics of brittle solids in compression. *Pure Appl. Geophys.* 133 (3), 489–521.
- Atkinson, B.K., 1980. Stress corrosion and the rate-dependent tensile failure of a fine-grained quartz rock. *Tectonophysics* 65, 281–290.
- Atkinson, B.K., 1984. Subcritical crack growth in geological materials. *J. Geophys. Res.* 89 (B6), 4077–4114.
- Atkinson, B.K., Meredith, P.G., 1981. Stress corrosion cracking of quartz: a note on the influence of chemical environment. *Tectonophysics* 77 (1–2), T1–T11.
- Atkinson, B.K., Meredith, P.G., 1987a. Experimental fracture mechanics data for rocks and minerals. In: Atkinson, B.K. (Ed.), *Fracture Mechanics of Rock*. Academic Press, London, pp. 477–525.
- Atkinson, B.K., Meredith, P.G., 1987b. The theory of subcritical crack growth with applications to minerals and rocks. In: Atkinson, B.K. (Ed.), *Fracture Mechanics of Rock*. Academic Press, London, pp. 111–116.
- Atkinson, B.K., 1982. Subcritical crack propagation in rocks: theory, experimental results and applications. *J. Struct. Geol.* 4, 41–56.
- Baud, P., Meredith, P.G., 1997. Damage accumulation during triaxial creep of Darley Dale sandstone from pore volumetry and acoustic emission. *Int. J. Rock Mech. Min. Sci.* 34 (3–4).
- Baud, P., Zhu, W., Wong, T.-F., 2000. Failure mode and weakening effect of water on sandstone. *J. Geophys. Res.* 105 (B7), 16371–16389.
- Bell, A.F., Naylor, M., Heap, M.J., Main, I.G., 2011. Forecasting volcanic eruptions and other material failure phenomena: an evaluation of the failure forecast method. *Geophys. Res. Lett.* 38, L15304. <http://dx.doi.org/10.1029/2011GL048155>.
- Bhat, H.S., Sammis, C.G., Rosakis, A.J., 2011. The micromechanics of Westerly granite at large compressive loads. *Pure Appl. Geophys.* 168 (12), 1–18.
- Brace, W.F., Paulding, B.W., Scholz, C.H., 1966. Dilatancy in the fracture of crystalline rocks. *J. Geophys. Res.* 71 (16), 3839–3953.
- Brantut, N., Heap, M.J., Baud, P., Meredith, P.G., 2012. Micromechanics of brittle creep in rocks. *J. Geophys. Res.* 117, B08412. <http://dx.doi.org/10.1029/2012JB009299>.
- Brudy, M., Zoback, M.D., Fuchs, K., Rummel, F., Baumgärtner, J., 1997. Estimation of the complete stress tensor to 8 km depth in the KTB scientific drill holes: implications for crustal strength. *J. Geophys. Res.* 102 (B8), 18453–18475.
- Charles, R.J., 1958. Static fatigue of glass. I. *J. Appl. Phys.* 29 (11), 1549–1553.
- Cogan, J., 1976. Triaxial creep tests of Ophongong limestone and Opir shale. *Int. J. Rock Mech. Min. Sci.* 13, 1–10.
- Coleman, B.D., 1958. Statistic and time dependence of mechanical breakdown in fibers. *J. Appl. Phys.* 29 (6), 968–983.
- Cook, N.G.W., 1981. Stiff testing machines, stick slip sliding, and the stability of rock deformation. In: Carter, N.L., Friedman, M., Logan, J.M., Stearns, D.W. (Eds.), *Mechanical Behavior of Crustal Rocks: The Handin Volume*. Geophys. Monogr. Ser., American Geophysical Union, Washington, DC, pp. 93–102.
- Cornet, T.H., Bérard, Th., Bourouis, S., 2007. How close to failure is a granite rock mass at a 5 km depth? *Int. J. Rock Mech. Min. Sci.* 44, 47–66.
- Costin, L.S., 1985. Damage mechanics in the post-failure regime. *Mech. Mat.* 4, 149–160.
- Costin, L.S., 1987. Time-dependent deformation and failure. In: Atkinson, B.K. (Ed.), *Fracture Mechanics of Rock*. Academic Press, London, pp. 167–215.
- Darot, M., Guéguen, Y., 1986. Slow crack growth in minerals and rocks: theory and experiments. *Pure Appl. Geophys.* 124 (4–5), 677–692.
- Deshpande, V.S., Evans, A.G., 2008. Inelastic deformation and energy dissipation in ceramics: a mechanism-based constitutive model. *J. Mech. Phys. Solids* 56 (10), 3077–3100.
- Diederichs, M.S., Kaiser, P.K., 1999. Tensile strength and abutment relaxation as failure control mechanisms in underground excavations. *Int. J. Rock Mech. Min. Sci.* 36 (1), 69–96.
- Freiman, S.W., 1984. Effects of chemical environments on slow crack growth in glasses and ceramics. *J. Geophys. Res.* 89 (B6), 4072–4076.
- Fujii, Y., Kiyama, T., Ishijima, Y., Kodama, J., 1999. Circumferential strain behavior during creep tests of brittle rocks. *Int. J. Rock Mech. Min. Sci.* 36, 323–337.
- Gasc-Barbier, M., Chanchole, S., Bérest, P., 2004. Creep behavior of Bure clayey rock. *Appl. Clay Sci.* 26, 449–458.
- Grgic, D., 2011. Influence of CO₂ on the long-term chemomechanical behavior of an oolitic limestone. *J. Geophys. Res.* 116, B07201. <http://dx.doi.org/10.1029/2010JB008176>.
- Griffith, A.A., 1921. The phenomena of rupture and flow in solids. *Phil. Trans. R. Soc. A* 221, 163–198.
- Hadizadeh, J., Law, R.D., 1991. Water-weakening of sandstone and quartzite deformed at various stress and strain rates. *Int. J. Rock Mech. Min. Sci.* 28 (5), 431–439.
- Heap, M.J., Baud, P., Meredith, P.G., Vinciguerra, S., Bell, A.F., Main, I.G., 2011. Brittle creep in basalt and its application to time-dependent volcano deformation. *Earth Planet. Sci. Lett.* 307, 71–82.
- Heap, M.J., Baud, P., Meredith, P.G., Bell, A.F., Main, I.G., 2009a. Time-dependent brittle creep in Darley Dale sandstone. *J. Geophys. Res.* 114, B07203. <http://dx.doi.org/10.1029/2008JB006212>.
- Heap, M.J., Baud, P., Meredith, P.G., 2009b. Influence of temperature on brittle creep in sandstones. *Geophys. Res. Lett.* 36. <http://dx.doi.org/10.1029/2009GL039373>.
- Hettema, M.H.H., de Pater, C.J., Wolf, K.-H.A.A., 1991. Effects of temperature and pore water on creep of sandstone rock. In: *The 32nd U. S. Symposium on Rock Mechanics*.
- Hirata, T., Satoh, T., Ito, K., 1987. Fractal structure of spatial distribution of microfracturing in rock. *Geophys. J. R. Astr. Soc.* 90, 369–374.
- Hoek, E., Bieniawski, Z.T., 1965. Rock fracture under static stress conditions. *Int. J. Fract.* 1 (3), 137–155.
- Irwin, G.R., 1958. *Fracture*. In: *Handbuch der Physik*, vol. 6. Springer, Berlin, pp. 551–590.
- Kachanov, M., 1993. Elastic solids with many cracks and related problems. In: Hutchinson, J.W., Wu, T.Y. (Eds.), *Advances in Applied Mechanics*, vol. 30. Academic Press, pp. 259–445.
- Kachanov, M., Sevostianov, I., 2012. Rice's internal variables formalism and its implications for the elastic and conductive properties of cracked materials, and for the attempts to relate strength to stiffness. *J. Appl. Mech.* 79 (3).
- Kachanov, M.L., 1982a. A microcrack model of rock inelasticity. Part I: frictional sliding on microcracks. *Mech. Mat.* 1, 19–27.
- Kachanov, M.L., 1982b. A microcrack model of rock inelasticity. Part II: propagation of microcracks. *Mech. Mat.* 1, 29–41.
- Kachanov, M.L., 1982c. A microcrack model of rock inelasticity. Part III: time-dependent growth of microcracks. *Mech. Mat.* 1, 123–129.
- Kemeny, J.M., 1991. A model for non-linear rock deformation under compression due to sub-critical crack growth. *Int. J. Rock Mech. Min. Sci. Geomech. Abstr.* 28 (6), 459–467.
- Kie, T.T., Quan, S.Z., Hai, Y.Z., Yang, W.X., 1989. Dilatancy, creep and relaxation of brittle rocks measured with the 8000 kN multipurpose triaxial apparatus. *Phys. Earth Planet. Int.* 55 (3–4), 335–352.
- King, G.C.P., Stein, R.S., Lin, J., 1994. Static stress changes and the triggering of earthquakes. *Bull. Seism. Soc. Am.* 84 (3), 935–953.
- Kranz, R.L., 1979. Crack growth and development during creep of Barre granite. *Int. J. Rock Mech. Min. Sci. Geomech. Abstr.* 16, 23–35.
- Kranz, R.L., 1980. The effects of confining pressure and stress difference on static fatigue of granite. *J. Geophys. Res.* 85 (B4), 1854–1866.
- Kranz, R.L., 1983. Microcracks in rocks: a review. *Tectonophysics* 100, 449–480.
- Kranz, R.L., Scholz, C.H., 1977. Critical dilatant volume of rocks at the onset of tertiary creep. *J. Geophys. Res.* 82 (30), 4893–4898.
- Kranz, R.L., Harris, W.J., Carter, N.L., 1982. Static fatigue of granite at 200 °C. *Geophys. Res. Lett.* 9 (1), 1–4.
- Kurita, K., Swanson, P.L., Getting, I.C., Spetzler, H., 1983. Surface deformation of Westerly granite during creep. *Geophys. Res. Lett.* 10 (1), 75–78.
- Lankford, J., 1981. The role of tensile microfracture in the strain rate dependence of compressive strength of fine-grained limestone – analogy with strong ceramics. *Int. J. Rock Mech. Min. Sci.* 18 (2), 173–175.
- Law, B.R., 1993. *Fracture of Brittle Solids*. Cambridge University Press, Cambridge [Eng.], New York.
- Lei, X., Kusunose, K., Rao, M.V.M.S., Nishizawa, O., Satoh, T., 2000. Quasi-static fault growth and cracking in homogeneous brittle rock under triaxial compression using acoustic emission monitoring. *J. Geophys. Res.* 105 (B3), 6127–6139.
- Lei, X., Kusunose, K., Satoh, T., Nishizawa, O., 2003. The hierarchical rupture process of a fault: an experimental study. *Phys. Earth Planet. Int.* 137, 213–228.
- Lemaitre, J., Chaboche, J.-L., 1990. *Mechanics of Solid Materials*. Cambridge University Press, Cambridge.
- Lockner, D.A., 1993a. Room temperature creep in saturated granite. *J. Geophys. Res.* 98 (B1), 475–487.
- Lockner, D.A., 1993b. The role of acoustic emission in the study of rock fracture. *Int. J. Rock Mech. Min. Sci. Geomech. Abstr.* 30 (7), 883–899.
- Lockner, D.A., 1998. A generalized law for brittle deformation of Westerly granite. *J. Geophys. Res.* 103 (B03), 5107–5123.
- Lockner, D.A., Byerlee, J.D., 1977. Acoustic emission and creep in rock at high confining pressure and differential stress. *Bull. Seism. Soc. Am.* 67 (2), 247–258.
- Lockner, D.A., Byerlee, J.D., 1986. Changes in complex resistivity during creep in granite. *Pure Appl. Geophys.* 124 (4–5), 659–676.

- Lockner, D.A., Madden, T.R., 1991a. A multiple crack model of brittle fracture. 1. Non-time-dependent simulations. *J. Geophys. Res.* 96 (B12), 19623–19642.
- Lockner, D.A., Madden, T.R., 1991b. A multiple crack model of brittle fracture. 2. Time-dependent simulations. *J. Geophys. Res.* 96 (B12), 19643–19654.
- Lockner, D.A., Byerlee, J.D., Kukensko, V., Ponomarev, A., Sidorin, A., 1992. Observation of quasi-static fault growth from acoustic emissions. In: Evans, B., Wong, T.F. (Eds.), *Fault Mechanics and Transport Properties of Rocks*. International Geophysics Series. Academic Press, London, pp. 3–31.
- Main, I.G., 1999. Applicability of time-to-failure analysis to accelerated strain before earthquakes and volcanic eruptions. *Geophys. J. Int.* 139 (3), F1–F6.
- Main, I.G., 2000. A damage mechanics model for power-law creep and earthquake aftershock and foreshock sequences. *Geophys. J. Int.* 142, 151–161.
- Main, I.G., Meredith, P.G., 1991. Stress corrosion constitutive laws as a possible mechanism of intermediate-term and short-term seismic quiescence. *Geophys. J. Int.* 107 (2), 363–372.
- Maranini, E., Brignoli, M., 1999. Creep behaviour of weak rock: experimental characterization. *Int. J. Rock Mech. Min. Sci.* 36, 127–138.
- Maranini, E., Yamaguchi, T., 2001. A non-associated viscoplastic model for the behaviour of granite in triaxial compression. *Mech. Mat.* 33, 283–293.
- Martin, R.J., Noel, J.S., Boyd, P.J., Price, R.H., 1997. Creep and static fatigue of welded tuff from Yucca mountain, Nevada. *Int. J. Rock Mech. Min. Sci.* 34, paper No. 190.
- Meredith, P.G., Atkinson, B.K., 1983. Stress corrosion and acoustic emission during tensile crack propagation in Whin Sill dolerite and other basic rocks. *Geophys. J. R. Astr. Soc.* 75 (1), 1–21.
- Meredith, P.G., Heap, M.J., Baud, P., Vinciguerra, S., Bell, A., Main, I.G., 2011. Brittle creep in rocks: from laboratory to crustal time scales. *Geophys. Res. Abstr.* 13. EGU2011-5906.
- Michalske, T.A., Freiman, S.W., 1982. A molecular interpretation of stress corrosion in silica. *Nature* 295, 511–512.
- Michalske, T.A., Freiman, S.W., 1983. A molecular mechanism for stress corrosion in vitreous silica. *J. Am. Ceram. Soc.* 66 (4), 284–288.
- Nara, Y., Takada, M., Mori, D., Owada, H., Yoneda, T., Kaneko, K., 2010. Applicability of time-to-failure analysis to accelerated strain before earthquakes and volcanic eruptions. *Int. J. Fract.* 164 (1), 57–71.
- Ngwenya, B.T., Main, I.G., Elphick, S.C., Crawford, B.R., Smart, B.G.D., 2001. A constitutive law for low-temperature creep of water-saturated sandstones. *J. Geophys. Res.* 106 (B10), 21811–21826.
- Niemeijer, A.R., Spiers, C.J., Bos, B., 2002. Compaction creep of quartz sand at 400–600 °C: experimental evidence for dissolution-controlled pressure solution. *Earth Planet. Sci. Lett.* 195, 261–275.
- Okubo, S., Fukui, K., Hashiba, K., 2008. Development of a transparent triaxial cell and observation of rock deformation in compression and creep tests. *Int. J. Rock Mech. Min. Sci.* 45, 351–361.
- Paterson, M.S., Wong, T.F., 2005. *Experimental Rock Deformation – The Brittle Field*, second ed. Springer-Verlag, Berlin Heidelberg.
- Perfettini, H., Avouac, J.-P., 2004. Postseismic relaxation driven by brittle creep: a possible mechanism to reconcile geodetic measurements and the decay rate of aftershocks, application to the Chi-Chi earthquake, Taiwan. *J. Geophys. Res.* 109, B02304. <http://dx.doi.org/10.1029/2003JB002488>.
- Rice, J.R., 1975. Continuum mechanics and thermodynamics of plasticity in relation to microscale deformation mechanisms. In: Argon, A.S. (Ed.), *Constitutive Equations in Plasticity*. MIT Press, Cambridge, MA.
- Rice, J.R., 1978. Thermodynamics of the quasi-static growth of Griffith cracks. *J. Mech. Phys. Solids* 26, 61–78.
- Ross, J.V., Bauer, S.J., Carter, N.L., 1983. Effect of the α - β quartz transition on the creep properties of quartzite and granite. *Geophys. Res. Lett.* 10 (12), 1129–1132.
- Røyne, A.R., Bisschop, J., Dysthe, D.K., 2011. Experimental investigation of surface energy and subcritical crack growth in calcite. *J. Geophys. Res.* 116, B04204. <http://dx.doi.org/10.1029/2010JB008033>.
- Rudnicki, J.W., Rice, J.R., 1975. Conditions for the localization of deformation in pressure-sensitive dilatant materials. *J. Mech. Phys. Solids* 23, 371–394.
- Rutter, E.H., 1983. Pressure solution in nature, theory and experiment. *J. Geol. Soc.* 140, 725–740.
- Rutter, E.H., Mainprice, D.H., 1978. The effect of water on stress relaxation of faulted and unfaulted sandstone. *Pure Appl. Geophys.* 116, 634–654.
- Sano, O., 1981. A note on the sources of acoustic emissions associated with subcritical crack growth. *Int. J. Rock Mech. Min. Sci. Geomech. Abstr.* 18, 259–263.
- Sano, O., Ito, I., Terada, M., 1981. Influence of strain rate on dilatancy and strength of Oshima granite under uniaxial compression. *J. Geophys. Res.* 86 (B10), 9299–9311.
- Satoh, T., Shivakumar, K., Nishizawa, O., Kusunose, K., 1996. Precursory localization and development of microfractures along the ultimate fracture plane in amphibolite under triaxial creep. *Geophys. Res. Lett.* 23 (8), 865–868.
- Scholz, C.H., 1968a. Experimental study of the fracturing process in brittle rock. *J. Geophys. Res.* 73 (4), 1447–1454.
- Scholz, C.H., 1968b. Mechanism of creep in brittle rock. *J. Geophys. Res.* 73 (10), 3295–3302.
- Scholz, C.H., 1972. Static fatigue of quartz. *J. Geophys. Res.* 77 (11), 2104–2114.
- Scholz, C.H., 2002. *The Mechanics of Earthquake and Faulting*, second ed. Cambridge University Press, Cambridge, United Kingdom.
- Sibson, R.H., 1986. Earthquakes and rock deformation in crustal fault zones. *Ann. Rev. Earth Planet. Sci.* 14, 149–175.
- Sih, G.C., 1973. *Handbook of Stress Intensity Factors*. Institute of Fracture and Solid Mechanics, Lehigh University, Bethlehem.
- Tada, H., Paris, P.C., Irwin, G.R., 1973. *The Stress Analysis of Cracks Handbook*. Del Research Corporation, Hellertown, Penna.
- Tapponnier, P., Brace, W.F., 1976. Development of stress-induced microcracks in Westerly granite. *Int. J. Rock Mech. Min. Sci. Geomech. Abstr.* 13, 103–112.
- Trippetta, F., Colletini, C., Barchi, M.R., Lupattelli, A., Mirabella, F., 2013. A multidisciplinary study of a natural example of a CO₂ geological reservoir in central Italy. *Int. J. Green. Gas Cont.* 12, 72–83.
- Tsai, L.S., Hsieh, Y.M., Weng, M.C., Huang, T.H., Jeng, F.S., 2008. Time-dependent deformation behaviors of weak sandstones. *Int. J. Rock Mech. Min. Sci.* 45, 144–154.
- Turcotte, D.L., Newman, W.I., Shcherbakov, R., 2003. Micro and macroscopic models of rock fracture. *Geophys. J. Int.* 152 (3), 718–728.
- Ventura, G., Vinciguerra, S., Moretti, S., Meredith, P.G., Heap, M.J., Baud, P., Shapiro, S.A., Dinske, C., Kummerow, J., 2010. Understanding slow deformation before dynamic failure. In: Beer, T., Mulder, E.F.J., Derbyshire, E. (Eds.), *Geophysical Hazards. International Year of Planet Earth*, vol. 5. Springer, Netherlands, pp. 229–247.
- Vinciguerra, S., Trovato, C., Meredith, P.G., Benson, P.M., 2005. Relating seismic velocities, thermal cracking and permeability in Mt. Etna and Iceland basalts. *Int. J. Rock Mech. Min. Sci.* 42 (7–8), 900–910.
- Waza, T., Kurita, K., Mizutani, H., 1980. The effect of water on the subcritical crack growth in silicate rocks. *Tectonophysics* 67, 25–34.
- Wan, K.-T., Lathabai, S., Lawn, B.R., 1990. Crack velocity functions and thresholds in brittle solids. *J. Eur. Ceram. Soc.* 6 (4), 259–268.
- Wiederhorn, S.M., Boltz, L.H., 1970. Stress corrosion and static fatigue of glass. *J. Am. Ceram. Soc.* 53 (10), 543–548.
- Wiederhorn, S.M., Johnson, H., 1972. Effect of electrolyte pH on crack propagation in glass. *J. Am. Ceram. Soc.* 56, 192–197.
- Wiederhorn, S.M., Freiman, S.W., Fuller, E.R., Simmons, C.J., 1982. Effects of water and other dielectrics on crack growth. *J. Mater. Sci.* 17 (12), 3460–3478.
- Wong, T.-F., Biegel, R., 1985. Effects of pressure on the micromechanics of faulting in San Marcos gabbro. *J. Struct. Geol.* 7 (6), 737–749.
- Wong, T.-F., David, C., Zhu, W., 1997. The transition from brittle faulting to cataclastic flow in porous sandstones: mechanical deformation. *J. Geophys. Res.* 102 (B2), 3009–3025.
- Wu, X.Y., Baud, P., Wong, T.-F., 2000. Micromechanics of compressive failure and spatial evolution of anisotropic damage in Darley Dale sandstone. *Int. J. Rock Mech. Min. Sci.* 37, 143–160.
- Xie, S.Y., Shao, J.F., Xu, W.Y., 2011. Effects of temperature and pore water on creep of sandstone rock. *Int. J. Rock Mech. Min. Sci.* 48, 741–747.
- Xu, T., Tang, C., Zhao, J., Li, L., Heap, M.J., 2012. Modelling the time-dependent rheological behaviour of heterogeneous brittle rocks. *Geophys. J. Int.* 189 (3), 1781–1796.
- Yang, S., Jiang, Y., 2010. Triaxial mechanical creep behavior of sandstone. *Min. Sci. Technol.* 20, 0339–0349.
- Yoshida, H., Horii, H., 1992. A micromechanics-based model for creep behavior of rock. *Appl. Mech. Rev.* 45 (8), 294–303.
- Zhang, Z.L., Xu, W.Y., Wang, W., Wang, R.B., 2012. Triaxial creep tests of rock from the compressive zone of dam foundation in Xiangjiaba Hydropower Station. *Int. J. Rock Mech. Min. Sci.* 50, 133–139.
- Zoback, M.L., Zoback, M.D., 1980. State of stress in the conterminous United States. *J. Geophys. Res.* 85 (B11), 6113–6156.
- Zoback, M.D., Healy, J.H., 1992. In situ stress measurements to 3.5 km depth in the Cajon pass scientific research borehole: Implication for the mechanics of crustal faulting. *J. Geophys. Res.* 97 (B4), 5039–5057.
- Zoback, M.D., Barton, C.A., Brudy, M., Castillo, D.A., Finkbeiner, T., Grollmund, B.R., Moos, D.B., Peska, P., Ward, C.D., Wiprut, D.J., 2003. Determination of stress orientation and magnitude in deep wells. *Int. J. Rock Mech. Min. Sci.* 40, 1049–1076.